



# On flame bifurcation and multiplicity in consistently propagating spherical flame and droplet evaporation fronts

Yijie Zhuang<sup>a</sup>, Huangwei Zhang<sup>b,\*</sup>

<sup>a</sup>School of Environmental Science and Engineering, Guangdong University of Technology, Guangzhou 510006, China

<sup>b</sup>Department of Mechanical Engineering, National University of Singapore, Singapore 117576, Singapore

## ARTICLE INFO

### Article history:

Received 1 October 2019

Revised 4 January 2020

Accepted 13 January 2020

Available online 16 January 2020

### Keywords:

Spherical flame

Droplet evaporation

Evaporative heat loss

Flame bifurcation

Markstein length

Lewis number

## ABSTRACT

The outwardly propagating spherical flames in premixed gas containing water droplets are theoretically studied in this work. The correlations between the flame propagation speed, droplet distribution and flame radius are derived, based on the large activation energy and quasi-planar flame assumptions. With this, flame bifurcation and multiplicity are analysed, focusing on the effects of initial droplet mass loading, evaporative heat loss and Lewis number. Meanwhile, the model can predict different gaseous flame types and liquid droplet distributions, as well as the bifurcations and transitions between them. It is shown that the spherical flame propagation is strongly affected by water droplet properties. When initial loading and/or heat loss coefficient are small, there is only one normal stable flame. Two stable flames arise when they increase, i.e. normal and weak flames. Increased droplet loading mainly affects the weak flame, resulting in decreased propagation speed, increased values of evaporation onset and completion fronts. However, increased heat loss affects both normal and weak flames, and flame bifurcation is observed for large heat loss. Droplet properties also greatly influence the weak flame transition between different regimes. Our results also show that Lewis number has significant influence on droplet-laden spherical flame propagation, in terms of flame bifurcation and regime transition. The Lewis number would affect the flame propagation jointly with the positive stretch rate and/or the evolving temperature gradients near the flame front through the interactions with the dispersed evaporating droplets. Furthermore, the magnitudes of Markstein length of the normal flames decrease when Lewis number approaches unity. However, those of the weak flames are mostly negative, indicating the enhancement over the shown Lewis number range. The larger magnitudes of Markstein length of weak flames show stronger sensitivity to stretch than those of normal flames. Finally, different flame types seen from our theoretical analysis are summarised.

© 2020 Elsevier Ltd. All rights reserved.

## 1. Introduction

Fire suppression systems and extinguishing media have attracted wide attention because of frequent fire and explosion hazards from industrial, civil and aerospace sectors. As a clean and economic agent, water mist is effective for fire suppression, and has been adopted for commercial practice (e.g. fire sprinklers) (Naito et al., 2011; Yang et al., 2004). Grant et al. (2000) and Liu and Kim (2000) review the state of the art regarding the applications of water sprays in fire protection engineering. Scientifically, fires or flames laden with sprayed water mist would involve complex two-phase combustion dynamics, due to the inter-

phase exchanges of mass, momentum, energy and chemical species (Lentati and Chelliah, 1998; Mitani, 1982a). The interpretation for their coupling can be made based on the thermal, physical and chemical effects from the dispersed water droplets. It is known that vaporization of liquid water to vapour can extract thermal energy (i.e. thermal effects) from the gas environment, and large quantities of water vapour may also reduce the oxygen concentration of the surrounding atmosphere (i.e. dilute effects) (Grant et al., 2000). Either of them is expected to considerably change the combustion characteristics of practical fire systems. Regarding the chemical effects, the water droplet can inhibit (Lentati and Chelliah, 1998) or promote (Babushok et al., 2015) the homogeneous chemical reaction pathways somehow. For instance, water vapour is expected to have higher three-body collision efficiency compared to other species (e.g. nitrogen), and hence enhances the radical recombination, which further weakens the combustion process (Lentati and Chelliah, 1998). However, overall, the chemical effects

\* Corresponding author at: Department of Mechanical Engineering, Faculty of Engineering, National University of Singapore, 9 Engineering Drive 1, Singapore 117576.

E-mail addresses: [syuzuzyj@163.com](mailto:syuzuzyj@163.com) (Y. Zhuang), [huangwei.zhang@nus.edu.sg](mailto:huangwei.zhang@nus.edu.sg) (H. Zhang).

## Nomenclature

$A$	pre-exponential factor of Arrhenius law
$C_p$	gas heat capacity
$d$	droplet diameter
$D$	gas molecular diffusivity
$D_{th}$	gas thermal diffusivity
$E$	activation energy
$H$	evaporation heat loss
$K$	stretch rate
$L$	Markstein length
$l_{th}$	flame thickness of an adiabatic planar flame
$Le$	Lewis number
$m$	mass
$N_d$	droplet number density
$q_v$	latent heat of vaporization
$q_c$	chemical reaction heat release
$Q$	ignition energy
$R^0$	universal gas constant
$R_f$	flame radius
$R_v$	vaporization front
$s_d$	droplet surface area
$t, r$	temporal and spatial coordinates
$T$	temperature
$T_b$	flame temperature of an adiabatic planar flame
$T_v$	boiling point
$u_b$	laminar flame speed of an adiabatic planar flame
$U$	flame propagation speed
$Y$	gas mass fraction
$Y_d$	droplet mass loading
$Z$	Zel'dovich number

### Greek letters

$\rho$	density
$\omega_v$	heat transfer rate
$\omega_c$	chemical reaction rate
$\lambda_g$	gas heat conductivity
$\eta$	moving coordinate attached to the propagating flame front
$\eta_v$	location of evaporation front in the moving coordinate
$\eta_{cp}$	location of evaporation completion front in the moving coordinate
$\Omega$	heat exchange coefficient
$\sigma$	thermal expansion ratio
$\delta$	initial droplet mass loading

### Superscripts

$\sim$	dimensional quantity
--------	----------------------

### Subscripts

$d$	corresponding to the liquid phase
$f$	at the flame front
$g$	corresponding to the gas phase
$v$	at the front of onset vaporization
$0$	in the fresh mixture
$U$	unburned zone
$B$	burned zone

### Acronym

ECF	Evaporation Completion Front
EOF	Evaporation Onset Front
FF	Flame Front

There have been some experimental (Ingram et al., 2013; Padilla et al., 2018; Sakurai et al., 2013; Sasongko et al., 2016; Vicariotto and Dunn, 2018; Yoshida et al., 2015; Yoshida et al., 2013) and numerical (Lee et al., 2017; Modak et al., 2006; Sarkar et al., 2019; Yang and Kee, 2002) studies on gaseous flames with water mists. For instance, Sakurai et al. (2013) experimentally investigate extinguishment of propane/air co-flowing diffusion flame by fine water droplets and their emphasis is laid on the effects of the water droplets on the flame base structures. Yoshida et al. (2015, 2013) conduct a series of experiments over a wider range of water mist diameters to investigate their influences on inhibition of counterflow methane/air diffusion flames. Their findings show that stretch rate and water mass fraction would jointly affect the flame extinction dynamics. Modak et al. (2006) and Yang and Kee (2002) simulate freely propagating hydrogen-, methane- and propane-air flames laden with water droplets. Based on their results, the optimum droplet size for reducing the burning velocity is about  $2 \mu\text{m}$  for hydrogen, while it is around  $10 \mu\text{m}$  for methane and propane. Recently, Lee et al. (2017) computationally investigate the extinction limits of counterflow non-premixed water-droplet-laden methane/air flames at various pressures. These observations, subject to specific fuels and droplet properties, are insightful to understand the influences of the water droplets in various flame configurations.

Through theoretical analysis, more general studies are conducted on the effects of droplet evaporation on the fundamental droplet-laden combustion processes. Dvorjetski and Greenberg investigate the effects of polydispersed water spray on extinction of counterflow polydispersed spray flames and gaseous diffusion flames (Dvorjetski and Greenberg, 2002, 2004). In their work, the effects of spray polydispersity on optimal flame suppression conditions are discussed. Blouquin and Joulin (1998) use asymptotic analysis to obtain a relation between the changes in burning rate, initial amount and size distribution of water droplets, and the gas properties/composition for steady planar flames. Belyakov et al. (2018) use linear stability analysis to analyse the laminar flame propagation and extinction in the gas mixture with monodispersed water mist by considering water droplet evaporation in pre-flame and post-flame zones.

In particular, due to the simple one-dimensional configuration, the spherical flame has been popularly investigated by asymptotic analysis to understand the general flame dynamics, e.g. in Refs. Chen and Ju (2007), Chen (2010), He (2000), Zhang and Chen (2011) and Zhang et al. (2013b). About two-phase situations, for example, Greenberg (2007) develops a theoretical model to evaluate the finite-rate fuel evaporation and droplet drag effects on spherical flame with liquid fuels. Then, Han and Chen (2015) apply the model suggested by Greenberg (2007) to investigate the effects of finite-rate fuel droplet evaporation on ignition and propagation of premixed spherical spray flame. Recently, Zhuang and Zhang (2019) derive a simplified theory for initiation, propagation and extinction of spherical flames with water droplets. Two scenarios are considered therein, corresponding to two different spatial distributions of water droplets. Significant phenomena are seen, for instance, regarding flame bifurcation and flammability limit resulting from the dispersed liquid droplets (Zhuang and Zhang, 2019).

In the above-mentioned investigations (except Ref. Belyakov et al., 2018), the dispersed droplets are always assumed to exist in the entire domain of interest. However, in practical situations, different properties of water droplets and local gas atmosphere may result in diverse droplet distributions and interactions with the local gas mixture (Grant et al., 2000). For example, small droplets are readily (fully) vaporized before the flame and their interactions with the reaction front are expected to be weak. Large droplets, however, may survive in the whole domain, and therefore simultaneously affect the hot burned zone

from the dispersed water droplets are relatively minor, compared to the other two (Lentati and Chelliah, 1998; Seshadri, 1978).

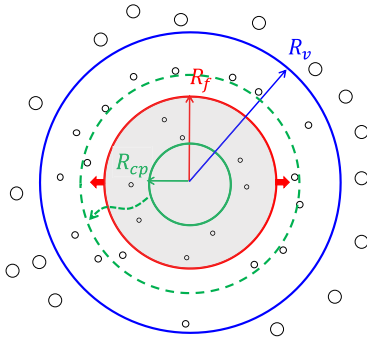


**Fig 1.** Schematic of outwardly propagating spherical flame with water droplet evaporation. The red line denotes the flame front ( $R_f$ ), whereas the open circles are the water droplets. The green solid and dashed lines respectively represent the fronts ( $R_{cp}$ ) at which the droplets completely vaporize behind or before the flame front. The blue line ( $R_v$ ) represents the front where the droplets start to evaporate. The shaded area corresponds to the burned zone. (For interpretation of the references to color in this figure legend, the reader is referred to the web version of this article.)

and fresh mixture zone. Furthermore, from the perspective of transient analysis, when the reaction front propagates, the droplet may preferentially finish the evaporation in some locations due to, e.g. the comparatively high local temperature and/or droplet Reynolds number. Obviously, this would lead to time-varying and spatially partial distributions of evaporating droplets before or behind the propagating flame front. Therefore, the interactions (e.g. evaporative heat loss) between the moving flame front and partially dispersed droplets are expected to be complicated, characterized by significant local and/or unsteady behaviours. Based on cloud bomb experiments, Bradley et al. (2014) analyse the relation between the spatial progress of droplet evaporation (i.e. whether droplets are fully vaporized in unburned or burned zone) and flame speed variations. Thimothée et al. (2017) experimentally investigate the passage of fuel droplets through a spherical two-phase flame and they find that the droplet size and the droplet inter-distance are the most important parameters which control the possibility for the droplet to penetrate the burnt gases. However, investigations on this problem are still limited, and therefore how the flame responds to the evolving distributions of the liquid droplet phase is not fully understood.

The present work aims to conduct the theoretical analysis based on premixed spherical laminar flames with water droplets. The focus is to examine the flame bifurcation and multiplicity

of the foregoing two-phase premixed reaction system, subject to the effects of droplet evaporation heat loss, initial mass loading and gas phase Lewis number. Compared to our previous analysis in Ref. Zhuang and Zhang (2019) and other theoretical studies (Greenberg, 2007; Han and Chen, 2015, 2016), the novelty of this work is that we consider the continuously evolving (therefore, fully or partially dispersed) distributions of evaporating droplets when the spherical flame propagates. The rest of the paper is structured as below. Mathematical model and theoretical analysis are presented in Sections 2 and 3, respectively. Results from the theoretical analysis will be discussed in detail in Section 4. Section 5 closes the paper with the main conclusions.

## 2. Mathematical model

The physical model and the typical flame structures in our work are shown in Figs. 1 and 2, respectively. A brief interpretation is presented below for the current physical model through comparing it with our previous models in Ref. Zhuang and Zhang (2019).

- (1) Firstly, different from the previous models with three zones (Greenberg, 2007; Han and Chen, 2015; Zhuang and Zhang, 2019), our model includes four zones (see Fig. 2) to describe droplet evaporation and fuel combustion, which are demarcated by the Evaporation Onset Front (EOF)  $R_v$ , Flame Front (FF)  $R_f$  and Evaporation Completion Front (ECF)  $R_{cp}$ . It should be noted that for  $R_v$  and  $R_{cp}$ , the term “front” is loosely used here to identify the locations where the droplets critically start and finish vaporization in our model. In Refs. Greenberg (2007), Han and Chen (2015) and Zhuang and Zhang (2019), only EOF and FF are considered.
- (2) Secondly, as the spherical flame propagates, the above characteristic fronts and their relative distance can continuously evolve, subject to the instantaneous coupling of the two phases. Specifically, in Fig. 1, EOF  $R_v$  corresponds to the location where the droplet starts to evaporate, which is defined when the droplet temperature reaches the boiling temperature. Note that EOF at  $R_v$  is always before the FF at  $R_f$ . Various evaporation capacities of water droplets may be presented in practical situations, depending on the droplet characteristics (e.g. diameter and mass loading) and evaporation rate (Belyakov et al., 2018). As such, the ECF  $R_{cp}$  may lie before or after the FF  $R_f$ , i.e.  $0 \leq R_{cp} < R_f$  (solid green line in Fig. 1) or  $R_{cp} > R_f$  (dashed green line in Fig. 1). Behind ECF, no droplets are left. For the former, it is termed as regime 1 hereafter, whereas for the

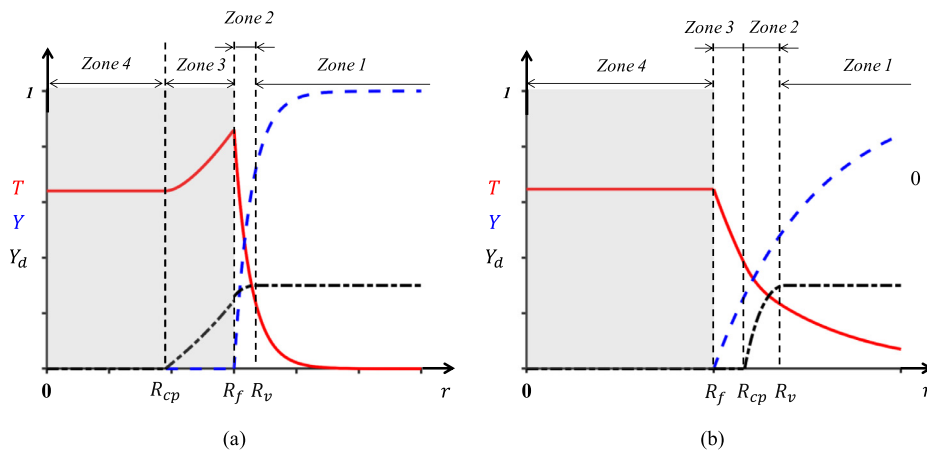


**Fig 2.** Schematic of four zones and the distributions of temperature and mass fractions in an outwardly propagating spherical flame with (a) droplets completely vaporize behind the flame front (regime 1) and (b) droplets completely vaporize before the flame front (regime 2).

latter, it is regime 2. Their flame structures are schematically demonstrated in Fig. 2(a) and (b), respectively.

- (3) Thirdly, this model can generally describe the evolutions of ECF through quantifying its movement initially from the spherical centre, leading to the transition from fully dispersed to partially dispersed droplet distributions in a propagating spherical flame. In Ref. Zhuang and Zhang (2019), this transition is not included, and the two cases studied in our previous work are the special solutions (i.e.  $R_{cp} = 0$  and  $R_{cp} = R_f$ , respectively) of the current model.

These three new features are expected to provide more detailed descriptions of droplet dynamics in the theoretical analysis, thereby rendering our model more general and flexible.

### 2.1. Governing equations

Eulerian descriptions are adopted for the droplet phase (Crow et al., 2011), in which case the droplet phase can be treated as an inter-penetrating medium. Like previous theoretical studies (Belyakov et al., 2018; Han and Chen, 2015, 2016; Blouquin and Joulin, 1998), the liquid droplets in the fuel-lean gaseous mixture with constant atmospheric pressure considered here are dilute, and therefore the interactions among them are negligible. Also, the inter-phasic kinetic equilibrium is assumed, and hence the droplets have the same velocities as gas phase. These simplifications were validated and popularly used in the previous analytical studies of gas-droplet reaction systems (Greenberg, 2007; Greenberg et al., 1996). Furthermore, in zone 1 (pre-vaporization) presented in Fig. 2, thermal equilibrium between droplets and fresh pre-mixture is assumed, and hence they have the same temperature (Belyakov et al., 2018; Han and Chen, 2015, 2016). Droplet evaporation critically occurs at the EOF  $R_v$  with boiling temperature. Behind this front, the droplet temperature maintains the boiling point and evaporation continues (Belyakov et al., 2018; Han and Chen, 2015, 2016). In addition, the droplet is assumed to be spherical and monodispersed. Note that, in this work, the possible droplet-induced flame front instability and the resultant variations of flame properties are not considered, which is typically caused by the full coupling between the gas and droplet phases.

The governing equation for droplet mass loading  $Y_d (= \tilde{N}_d \tilde{m}_d / \tilde{\rho}_g)$ , one can obtain the Eulerian equation for  $Y_d$

$$\frac{\partial}{\partial \tilde{t}} \left( \frac{\tilde{N}_d \tilde{m}_d}{\tilde{\rho}_g} \right) = \frac{\partial Y_d}{\partial \tilde{t}} = -\frac{\tilde{\omega}_m}{\tilde{\rho}_g}, \quad (1)$$

in which  $\tilde{\rho}_g$  is density of the local gaseous mixture,  $\tilde{\omega}_m$  is droplet evaporation rate and  $\tilde{N}_d$  is droplet number density. Here we further assume that the heat transferred from the surrounding gas to the droplets is completely used for phase change, which is related to the latent heat of evaporation  $\tilde{q}_v$  (Hayashi and Kumagai, 1975; Belyakov et al., 2018; Zhuang and Zhang, 2019). Therefore,  $\tilde{\omega}_m$  in Eq. (1) can be estimated from the heat transfer rate  $\tilde{\omega}_v$

$$\tilde{\omega}_m = \frac{\tilde{\omega}_v}{\tilde{q}_v} = \frac{1}{\tilde{q}_v} \tilde{N}_d \tilde{h} \tilde{s}_d (\tilde{T} - \tilde{T}_v). \quad (2)$$

Here  $\tilde{s}_d = \pi \tilde{d}^2$  is the droplet surface area with  $\tilde{d}$  being the droplet diameter.  $\tilde{T}$  is the gas temperature, whilst  $\tilde{T}_v$  is the boiling temperature.  $\tilde{h}$  is the heat transfer coefficient, which is estimated using the following correlation from Ranz and Marshall (1952)

$$Nu = \frac{\tilde{h} \tilde{d}}{\tilde{\lambda}_g} = 2.0 + 0.6 Re^{1/2} Pr^{1/3}, \quad (3)$$

where  $\tilde{\lambda}_g$  is the thermal conductivity.  $Nu$ ,  $Pr$  and  $Re$  are the Nusselt number, Prandtl number and droplet Reynolds number, respectively. Here  $Re$  is defined as  $Re = \tilde{\rho}_d \tilde{d} |\tilde{u}_g - \tilde{u}_d| / \tilde{\mu}_g$ , where  $\tilde{\rho}_d$  is the

droplet material density,  $\tilde{\mu}_g$  is the gaseous mixture dynamic viscosity and  $\tilde{u}_g$  and  $\tilde{u}_d$  are the velocities for gas and liquid phases, respectively. We can neglect the effects of droplet Reynolds number in Eq. (3) due to the assumption of kinetic equilibrium and therefore  $Nu \approx 2$  is assumed. Accordingly, the evaporation rate  $\tilde{\omega}_m$  in Eq. (2) can be rewritten as  $\tilde{\omega}_m = 2 \tilde{N}_d \tilde{\lambda}_g \tilde{s}_d (\tilde{T} - \tilde{T}_v) / (\tilde{q}_v \tilde{d})$ .

It should be noted that differences exist between the current evaporation model (i.e. Eq. 2) and those presented in Ref. Sazhin (2006), in which  $\tilde{\omega}_m$  is typically a function of Sherwood number, Spalding mass transfer number, as well as gas and droplet properties (density and diameter). For the studied problems in this work, since the kinetic equilibrium assumption is adopted, and hence it can be expected that the effects of the Sherwood number is small. Furthermore, since it is assumed that evaporation proceeds at the boiling temperature and constant atmospheric pressure, the water vapour at the droplet surface is relatively constant and hence the Spalding number would change slightly. Differently, the current model, Eq. (2), is based on the assumption of energy balance between phase change and heat transfer with the gaseous mixture. Essentially, it also considers the various effects of the gas and liquid phase properties and hence is physically comprehensive. In this work, only the evaporative cooling on the dynamics of fuel-lean flames will be studied, see Eqs. (4) and (5). Therefore, the current evaporation model is expected to be sufficient. This can also be confirmed by the previous theoretical work with the same model (Belyakov et al., 2018; Zhuang and Zhang, 2019), from which the physically sound critical flame phenomena have been unveiled.

For gas phase, we adopt the well-known diffusive-thermal model (Joulin et al., 1979), according to which the density, thermal and transport properties are assumed to be constant. The validity of the constant thermal property assumption has been confirmed in the previous detailed numerical simulations of gaseous propagating spherical flames (Chen and Ju, 2007; Li et al., 2018; Zhang and Chen, 2011; Zhang et al., 2013a). Furthermore, since the liquid droplets are dilute and their mass concentration is sufficiently small, the transport properties are assumed to be not affected by their presence (Belyakov et al., 2018; Greenberg, 2007; Han and Chen, 2015). Hence, the gas motion induced by thermal-expansion and droplet evaporation are neglected. These simplifications were also used in previous analytical studies of both gaseous flames and two-phase flames with dispersed liquid droplets (Chen and Ju, 2007; Chen et al., 2009; Han and Chen, 2015, 2016; He, 2000; Zhang and Chen, 2011; Zhang et al., 2013b, a; Chen et al., 2011) and reasonable results are obtained for the general features of spherical flames with droplets. As such, the governing equations for temperature and fuel mass fraction of gas phase respectively are

$$\tilde{\rho}_g \tilde{C}_p \frac{\partial \tilde{T}}{\partial \tilde{t}} = \frac{1}{\tilde{r}^2} \frac{\partial}{\partial \tilde{r}} \left( \tilde{r}^2 \tilde{\lambda}_g \frac{\partial \tilde{T}}{\partial \tilde{r}} \right) + \tilde{q}_c \tilde{\omega}_c - \tilde{\omega}_v, \quad (4)$$

$$\tilde{\rho}_g \frac{\partial \tilde{Y}}{\partial \tilde{t}} = \frac{1}{\tilde{r}^2} \frac{\partial}{\partial \tilde{r}} \left( \tilde{r}^2 \tilde{\rho}_g \tilde{D} \frac{\partial \tilde{Y}}{\partial \tilde{r}} \right) - \tilde{\omega}_c, \quad (5)$$

where  $\tilde{r}$  is the radius, and  $\tilde{Y}$  is the fuel mass fraction.  $\tilde{\rho}_g$ ,  $\tilde{C}_p$  and  $\tilde{D}$  are the density, heat capacity and molecular diffusivity of the gaseous fuel, respectively.  $\tilde{q}_c$  is chemical reaction heat release per unit mass of fuel.  $\tilde{\omega}_c$  is the reaction rate for one-step irreversible reaction and is calculated as

$$\tilde{\omega}_c = \tilde{\rho}_g \tilde{A} \tilde{Y} \exp(-\tilde{E} / \tilde{R}^0 \tilde{T}), \quad (6)$$

where  $\tilde{A}$  is the pre-exponential factor of Arrhenius law,  $\tilde{E}$  is the activation energy, and  $\tilde{R}^0$  is the universal gas constant. Besides, radiation heat transfer is not included in this work.

We introduce the following non-dimensional variables

$$U = \frac{\tilde{u}}{\tilde{u}_b}, r = \frac{\tilde{r}}{\tilde{l}_{th}}, t = \frac{\tilde{t}}{\frac{\tilde{l}_{th}}{\tilde{u}_b}}, Y = \frac{\tilde{Y}}{\tilde{Y}_0}, T = \frac{\tilde{T} - \tilde{T}_0}{\tilde{T}_b}. \quad (7)$$

Here  $\tilde{T}_0$  and  $\tilde{Y}_0$  denote the temperature and fuel mass fraction in the fresh mixture, respectively.  $\tilde{u}_b, \tilde{T}_b = \tilde{q}_c \tilde{Y}_0 / \tilde{C}_p, \tilde{l}_{th} = \tilde{D}_{th} / \tilde{u}_b$  are the laminar flame speed, flame temperature and flame thickness of an adiabatic planar flame without water mist addition, respectively.  $\tilde{D}_{th} = \tilde{\lambda}_g / (\tilde{\rho}_g \tilde{C}_p)$  is the gas thermal diffusivity.

As shown in the previous theoretical analysis for both gaseous flames and two-phase flames with dispersed liquid droplets (Chen and Ju, 2007; Chen et al., 2009; Han and Chen, 2015, 2016; He, 2000; Zhang and Chen, 2011; Zhang et al., 2013b, a; Chen et al., 2011), it is reasonable to adopt the quasi-steady state assumption in the moving coordinate system attached to the stably propagating flame front  $R_f(t)$ , i.e.  $\eta = r - R_f(t)$ . This assumption has been validated by transient numerical simulations for gaseous spherical flames without droplets (Chen and Ju, 2007; He, 2000; Li et al., 2018; Zhang and Chen, 2011), in which the unsteady effects are found to have a negligible influence in light of the overall balance between diffusion, reaction and convection processes in stably propagating spherical flames. Due to relatively dilute water droplet concentration and the chemically inert characteristics, the influences of water droplets on the flame zone thickness are small and therefore gaseous combustion still dominates in the studied problem (Belyakov et al., 2018; Han and Chen, 2015). In addition, due to the kinetic equilibrium between two phases, the droplets approximately follow the motion of the gas phase. Therefore, the quasi-steady state assumption in  $\eta$  coordinate system will be adopted for both gas and droplet equations in the present analysis. The non-dimensional form of the gas and droplet equations, i.e. Eqs. (3)–(5), under the quasi-steady state assumption ( $\partial/\partial t = 0$ ), reads

$$-U \frac{dT}{d\eta} = \frac{1}{(\eta + R_f)^2} \frac{d}{d\eta} \left[ (\eta + R_f)^2 \frac{dT}{d\eta} \right] + \omega_c - \omega_v, \quad (8)$$

$$-U \frac{dY}{d\eta} = Le^{-1} \frac{1}{(\eta + R_f)^2} \frac{d}{d\eta} \left[ (\eta + R_f)^2 \frac{dY}{d\eta} \right] - \omega_c, \quad (9)$$

$$-U \frac{dY_d}{d\eta} = -\frac{\omega_v}{q_v}, \quad (10)$$

where  $U = dR_f(t)/dt$  is the non-dimensional flame propagating speed and  $Le = \tilde{D}_{th} / \tilde{D}$  is the Lewis number. The normalized latent heat of vaporization is  $q_v = \tilde{q}_v / (\tilde{C}_p \tilde{T}_b)$ , and the chemical reaction is  $\omega_c = \tilde{l}_{th} \tilde{\omega}_c / (\tilde{\rho}_g \tilde{u}_b \tilde{Y}_0)$ . Additionally, the non-dimensional interphase heat transfer rate  $\omega_v$  is

$$\omega_v = \Omega(T - T_v). \quad (11)$$

Here  $T_v$  is the non-dimensional boiling temperature, the heat exchange coefficient  $\Omega$  in Eq. (10) is

$$\Omega = \pi \tilde{N}_d \tilde{Nud} \tilde{D}_{th}^2 \tilde{u}_b^{-2}. \quad (12)$$

As shown in Eq. (12), the non-dimensional parameter  $\Omega$  essentially is a gross parameter affected by both gas and droplet properties (Belyakov et al., 2018; Zhuang and Zhang, 2019). To avoid the nonlinearity in Eq. (10), note that we do not include the dependence of  $\Omega$  on  $Y_d$  ( $\Omega \sim Y_d^{1/3}$ ) and consider  $d$  as a constant, which is also done by Belyakov et al. (2018).

In the current work, propagation of the droplet-laden spherical flames under moderate and weak stretch rate conditions will be considered. Therefore, like Refs. Bechtold et al. (2005), Bechtold and Matalon (1987), Law (2006), Chen et al. (2009), Chung and Law (1988), Frankel and Sivashinsky (1984), Ronney and Sivashinsky (1989) and Zhang et al. (2013b), we assume that the

reactive-diffusive structure of the propagating spherical flame is quasi-planar ( $R_f \gg 1$ ) in this study. Therefore, Eqs. (8)–(10) can be reduced to

$$\frac{d^2 T}{d\eta^2} + \left( \frac{2}{R_f} + U \right) \frac{dT}{d\eta} + \omega_c - \omega_v = 0, \quad (13)$$

$$\frac{d^2 Y}{d\eta^2} + \left( \frac{2}{R_f} + LeU \right) \frac{dY}{d\eta} - Le\omega_c = 0, \quad (14)$$

$$-U \frac{dY_d}{d\eta} = -\frac{\omega_v}{q_v}. \quad (15)$$

The validity of the above assumption ( $R_f \gg 1$ ) in studying the spherical flame propagation has been confirmed in Refs. Bechtold et al. (2005), Bechtold and Matalon (1987), Law (2006), Chen et al. (2009), Chung and Law (1988), Frankel and Sivashinsky (1984), Ronney and Sivashinsky (1989) and Zhang et al. (2013b), through comparing the flame propagating speeds predicted by more detailed theories or numerical simulations.

## 2.2. Jump and boundary conditions

The non-dimensional boundary conditions for both gas phase ( $T$  and  $Y$ ) and droplet phase ( $Y_d$ ) equations at the spherical centre ( $\eta = -R_f$ ) and in the fresh mixture ( $\eta \rightarrow \infty$ ) are

$$\eta = -R_f : \frac{dT}{d\eta} = 0, \frac{dY}{d\eta} = 0, Y_d = 0. \quad (16)$$

$$\eta \rightarrow \infty : T = 0, Y = 1, Y_d = \delta. \quad (17)$$

Here  $\delta$  is the initial mass loading of the water droplets in the fresh mixture.

At the EOF,  $\eta = \eta_v = R_v - R_f$ , the temperature  $T$ , fuel mass fraction  $Y$  and droplet mass loading  $Y_d$  satisfy the following jump conditions (Belyakov et al., 2018; Han and Chen, 2015, 2016)

$$T = T_v, [Y] = [T] = \left[ \frac{dY}{d\eta} \right] = \left[ \frac{dT}{d\eta} \right] = 0, [Y_d] = 0. \quad (18)$$

At the ECF,  $\eta = \eta_{cp} = R_{cp} - R_f$ , the temperature  $T$ , fuel mass fraction  $Y$  and droplet mass loading  $Y_d$  satisfy the following jump conditions (Belyakov et al., 2018)

$$\begin{cases} [Y] = [T] = \left[ \frac{dY}{d\eta} \right] = \left[ \frac{dT}{d\eta} \right] = 0, [Y_d] = 0, & \text{if } \eta_{cp} > 0 \\ [T] = 0, \frac{dT^+}{d\eta} = 0, [Y_d] = 0. & \text{if } \eta_{cp} < 0 \end{cases} \quad (19)$$

The superscript “+” denotes the value from the side of oncoming gas flow. As mentioned above, in our previous work (Zhuang and Zhang, 2019), the ECF is assumed to coincide with the flame front or the spherical centre, and therefore the above jump conditions, i.e. Eq. (19), are not enforced.

In the limit of large activation energy, chemical reactions in gas phase are confined at an infinitesimally thin flame sheet (i.e.  $\eta = 0$ ) (Chen and Ju, 2007; Joulin et al., 1979). Therefore, the corresponding jump conditions at FF, i.e.  $\eta = 0$ , are (Han and Chen, 2015, 2016)

$$\begin{aligned} T = T_f, Y = 0, [Y_d] = 0, -\left[ \frac{dT}{d\eta} \right] &= Le^{-1} \left[ \frac{dY}{d\eta} \right] \\ &= [\sigma + (1 - \sigma)T_f]^2 \exp \left[ \frac{Z}{2} \left( \frac{T_f - 1}{\sigma + (1 - \sigma)T_f} \right) \right], \end{aligned} \quad (20)$$

where  $T_f$  is the flame temperature,  $\sigma$  is the thermal expansion ratio and  $Z$  is the Zel'dovich number. In Eq. (20),  $Y = 0$  is seen as the appropriate condition for the present nonadiabatic flame sheet model with evaporative heat loss. The square brackets, i.e.  $[f] = f(\eta^+) - f(\eta^-)$ , denote the difference between the variables at two sides of the EOF ( $\eta = \eta_v$ ) or ECF ( $\eta = \eta_{cp}$ ) or FF ( $\eta = 0$ ).

### 3. Theoretical analysis

Eqs. (13)–(15) with proper jump and boundary conditions in Section 2.2 are solved analytically in zones 1, 2, 3 and 4 (as shown in Fig. 2), respectively. They will be presented below in terms of the solutions of the above system, as well as the correlations between flame propagating speed and radius.

#### 3.1. Distributions of fuel mass fraction, droplet mass loading and temperature

The solutions for fuel mass fraction,  $Y$ , in zones 1–4 are (Note that the subscripts for  $Y$  denote the zone indices shown in Fig. 2, which also applies for  $Y_d$  and  $T$ )

$$Y_{1,2} = 1 - \exp\left(-\frac{2 + LeR_f U}{R_f} \eta\right), \quad (21)$$

$$Y_{3,4} = 0. \quad (22)$$

The solutions for droplet mass loading,  $Y_d$ , in zones 1–4 are

$$Y_{d1} = \delta, \quad (23)$$

$$Y_{d2} = \delta + T_v \frac{\Omega}{Uq_v} \frac{2 + R_f U}{R_f(\gamma_a - \gamma_b)} \times \left\{ \frac{\exp[\gamma_b(\eta - \eta_v)] - 1}{\gamma_b} - \frac{\exp[\gamma_a(\eta - \eta_v)] - 1}{\gamma_a} \right\}, \quad (24)$$

$$Y_{d3} = \begin{cases} 0, & \text{if } \eta_{cp} > 0 \\ \frac{\Omega}{Uq_v} \frac{T_f - T_v}{\frac{\exp(-\gamma_a \eta_{cp})}{\gamma_a} - \frac{\exp(-\gamma_b \eta_{cp})}{\gamma_b}}, & \text{if } \eta_{cp} < 0 \end{cases} \left\{ \frac{\exp[\gamma_a(\eta - \eta_{cp})] - 1}{\gamma_a \gamma_a} - \frac{\exp[\gamma_b(\eta - \eta_{cp})] - 1}{\gamma_b \gamma_b} \right\}, \quad (25)$$

$$Y_{d4} = 0, \quad (26)$$

where  $\gamma_{a,b} = 0.5[-\frac{2}{R_f} - U \pm \sqrt{4\Omega + \frac{(2+R_f U)^2}{R_f^2}}]$ .

The solutions for gas temperature,  $T$ , in zones 1–4 are

$$T_1 = T_v \exp\left[-\frac{2 + R_f U}{R_f} (\eta - \eta_v)\right], \quad (27)$$

$$T_2 = T_v - T_v \frac{2 + R_f U}{R_f(\gamma_a - \gamma_b)} \{ \exp[\gamma_a(\eta - \eta_v)] - \exp[\gamma_b(\eta - \eta_v)] \}, \quad (28)$$

$$T_3 = \begin{cases} T_v - T_v \frac{2 + R_f U}{R_f(\gamma_a - \gamma_b)} \{ \exp[\gamma_a(\eta_{cp} - \eta_v)] - \exp[\gamma_b(\eta_{cp} - \eta_v)] \} \\ + T_v \frac{1}{\gamma_a - \gamma_b} \{ \gamma_a \exp[\gamma_a(\eta_{cp} - \eta_v)] - \gamma_b \exp[\gamma_b(\eta_{cp} - \eta_v)] \} \\ \left\{ \exp\left[\frac{2 + R_f U}{R_f} (\eta_{cp} - \eta)\right] - 1 \right\}, & \text{if } \eta_{cp} > 0 \\ T_v + \frac{T_f - T_v}{\frac{\exp(-\gamma_a \eta_{cp})}{\gamma_a} - \frac{\exp(-\gamma_b \eta_{cp})}{\gamma_b}} \left\{ \frac{\exp[\gamma_a(\eta - \eta_{cp})]}{\gamma_a} - \frac{\exp[\gamma_b(\eta - \eta_{cp})]}{\gamma_b} \right\}, & \text{if } \eta_{cp} < 0 \end{cases} \quad (29)$$

$$T_4 = \begin{cases} T_f, & \text{if } \eta_{cp} > 0 \\ T_v + \frac{T_f - T_v}{\frac{\exp(-\gamma_a \eta_{cp})}{\gamma_a} - \frac{\exp(-\gamma_b \eta_{cp})}{\gamma_b}} \left\{ \frac{1}{\gamma_a} - \frac{1}{\gamma_b} \right\}, & \text{if } \eta_{cp} < 0 \end{cases} \quad (30)$$

#### 3.2. Correlations for propagating spherical flames with water droplets

Based on the jump conditions in Eq. (20), one obtains the following algebraic system for the correlations between flame temperature  $T_f$ , flame propagating speed  $U$ , flame radius  $R_f$ , EOF  $\eta_v$  and ECF  $\eta_{cp}$ :

If the droplets evaporate completely in the combustion products, i.e.  $-R_f \leq \eta_{cp} < 0$  in regime 1, then the correlation reads

$$T_v \frac{2 + R_f U}{R_f(\gamma_a - \gamma_b)} \{ \gamma_a \exp[\gamma_a(-\eta_v)] - \gamma_b \exp[\gamma_b(-\eta_v)] \} + \frac{T_f - T_v}{\frac{\exp(-\gamma_a \eta_{cp})}{\gamma_a} - \frac{\exp(-\gamma_b \eta_{cp})}{\gamma_b}} \{ \exp[\gamma_a(-\eta_{cp})] - \exp[\gamma_b(-\eta_{cp})] \} = \frac{2 + LeR_f U}{LeR_f} = [\sigma + (1 - \sigma)T_f]^2 \exp\left[\frac{Z}{2} \frac{T_f - 1}{\sigma + (1 - \sigma)T_f}\right], \quad (31)$$

$$T_f = T_v - T_v \frac{2 + R_f U}{R_f(\gamma_a - \gamma_b)} \{ \exp[\gamma_a(-\eta_v)] - \exp[\gamma_b(-\eta_v)] \}, \quad (32)$$

$$\delta + T_v \frac{\Omega}{Uq_v} \frac{2 + R_f U}{R_f(\gamma_a - \gamma_b)} \left\{ \frac{\exp[\gamma_b(-\eta_v)] - 1}{\gamma_b} - \frac{\exp[\gamma_a(-\eta_v)] - 1}{\gamma_a} \right\} = \frac{\Omega}{Uq_v} \frac{T_f - T_v}{\frac{\exp(-\gamma_a \eta_{cp})}{\gamma_a} - \frac{\exp(-\gamma_b \eta_{cp})}{\gamma_b}} \left\{ \frac{\exp[\gamma_a(-\eta_{cp})] - 1}{\gamma_a \gamma_a} - \frac{\exp[\gamma_b(-\eta_{cp})] - 1}{\gamma_b \gamma_b} \right\}. \quad (33)$$

If the droplets evaporate completely before the FF, i.e.  $\eta_{cp} > 0$  in regime 2, then the correlation reads

$$T_v \frac{2 + R_f U}{R_f(\gamma_a - \gamma_b)} \{ \gamma_a \exp[\gamma_a(\eta_{cp} - \eta_v)] - \gamma_b \exp[\gamma_b(\eta_{cp} - \eta_v)] \} \exp\left(\frac{2 + R_f U}{R_f} \eta_{cp}\right) = \frac{2 + LeR_f U}{LeR_f} = [\sigma + (1 - \sigma)T_f]^2 \exp\left[\frac{Z}{2} \frac{T_f - 1}{\sigma + (1 - \sigma)T_f}\right], \quad (34)$$

$$T_f = T_v - T_v \frac{2 + R_f U}{R_f(\gamma_a - \gamma_b)} \{ \exp[\gamma_a(\eta_{cp} - \eta_v)] - \exp[\gamma_b(\eta_{cp} - \eta_v)] \} + T_v \frac{1}{\gamma_a - \gamma_b} \{ \gamma_a \exp[\gamma_a(\eta_{cp} - \eta_v)] - \gamma_b \exp[\gamma_b(\eta_{cp} - \eta_v)] \} \left\{ \exp\left(\frac{2 + R_f U}{R_f} \eta_{cp}\right) - 1 \right\}, \quad (35)$$

$$\delta + T_v \frac{\Omega}{Uq_v} \frac{2 + R_f U}{R_f(\gamma_a - \gamma_b)} \left\{ \frac{\exp[\gamma_b(\eta_{cp} - \eta_v)] - 1}{\gamma_b} - \frac{\exp[\gamma_a(\eta_{cp} - \eta_v)] - 1}{\gamma_a} \right\} = 0. \quad (36)$$

Eqs. (31)–(33), as well as Eqs. (34)–(36), describe the correlations between flame propagation speed  $U$ , radius  $R_f$ , temperature  $T_f$ , EOF  $\eta_v$  and ECF  $\eta_{cp}$  when the droplet-laden spherical flames

propagate outwardly with  $-R_f \leq \eta_{cp} < 0$  (regime 1) and  $\eta_{cp} > 0$  (regime 2), respectively. Note that due to the existence of the ECF location  $\eta_{cp}$  in the current model, the system of the correlation would have four equations, instead of three in our previous work (Zhuang and Zhang, 2019). For droplet dynamics, this theory can describe the evolutions from fully dispersed to partially dispersed conditions, and also the transitions from regime 1 to regime 2 for the interactions between ECF and FF in propagating spherical flames. Various parameters are included in the foregoing equations, including Lewis number ( $Le$ ), heat exchange coefficient ( $\Omega$ ), and initial droplet mass loading ( $\delta$ ). Therefore, their effects on propagation of spherical flames can be discussed through numerically solving Eqs. (31)–(36).

The current model can recover the correlations for droplet-free spherical flames (Chen and Ju 2007) in the limit of  $\delta \rightarrow 0$ . In addition, when the flame radius tends to be infinite ( $R_f \rightarrow +\infty$ ), the current model can be reduced into that for two-phase planar flames from Ref. Belyakov et al. (2018). In particular, when  $\eta_{cp} = 0$  (i.e. ECF critically lies at FF), Eqs. (31)–(33) and Eqs. (34)–(36) can be simplified into the unified form, i.e.

$$T_v \frac{2 + R_f U}{R_f (\gamma_a - \gamma_b)} \{ \gamma_a \exp[\gamma_a (-\eta_v)] - \gamma_b \exp[\gamma_b (-\eta_v)] \} = \frac{2 + Le R_f U}{Le R_f} = [ \sigma + (1 - \sigma) T_f ]^2 \exp \left[ \frac{Z}{2} \frac{T_f - 1}{\sigma + (1 - \sigma) T_f} \right], \quad (37)$$

$$T_f = T_v - T_v \frac{2 + R_f U}{R_f (\gamma_a - \gamma_b)} \{ \exp[\gamma_a (-\eta_v)] - \exp[\gamma_b (-\eta_v)] \}, \quad (38)$$

$$\delta + T_v \frac{\Omega}{U q_v} \frac{2 + R_f U}{R_f (\gamma_a - \gamma_b)} \left\{ \frac{\exp[\gamma_b (-\eta_v)] - 1}{\gamma_b} - \frac{\exp[\gamma_a (-\eta_v)] - 1}{\gamma_a} \right\} = 0. \quad (39)$$

Eqs. (37)–(39) are the same as the correlations in which the droplets are critically completely vaporized in the reaction sheet, i.e. case 1 in our previous analysis (Zhuang and Zhang, 2019) under the quasi-planar assumption of  $R_f \gg 1$ . Besides, case 2 in our previous analysis (Zhuang and Zhang, 2019) can also be captured by the present model, i.e. when initial droplet mass loading  $\delta$  is relatively large, the droplets are fully distributed in the burned zone, and therefore the ECF remains in the spherical centre in the early stage of flame propagation, i.e.  $\eta_{cp} = -R_f$ .

#### 4. Results and discussion

The constants of the correlations used for the following analysis include (Belyakov et al., 2018; Chen and Ju, 2007): Zeldovich number  $Z = 10$ , thermal expansion ratio  $\sigma = 0.15$ , normalized boiling point of water  $T_v = 0.222$ , normalized latent heat of water evaporation  $q_v = 1.256$ . Note that these values of  $T_v$  and  $q_v$  correspond to the properties of liquid water at atmospheric pressure (Belyakov et al., 2018). Noted that in the present study the influence of the properties of the fuel-air mixture on the  $q_v$  is not considered as done by Belyakov et al. (2018) and Han and Chen (2015).

##### 4.1. Droplet-laden propagating planar flames

The planar flame ( $R_f \rightarrow +\infty$ ) is the limiting case of the moderately or weakly stretched spherical flame studied in this work, and therefore understanding the behaviours of the former would be conducive for our ensuring analysis of the latter. The dependencies of flame propagation speed  $U$  on heat transfer coefficient  $\Omega$  at different mass loadings  $\delta$  with  $Le = 1.0$  for the planar flame are shown in Fig. 3. These solutions are obtained by assuming the flame radius is infinite large (i.e.  $R_f \rightarrow +\infty$ ) in the correlations from Section 3.2.

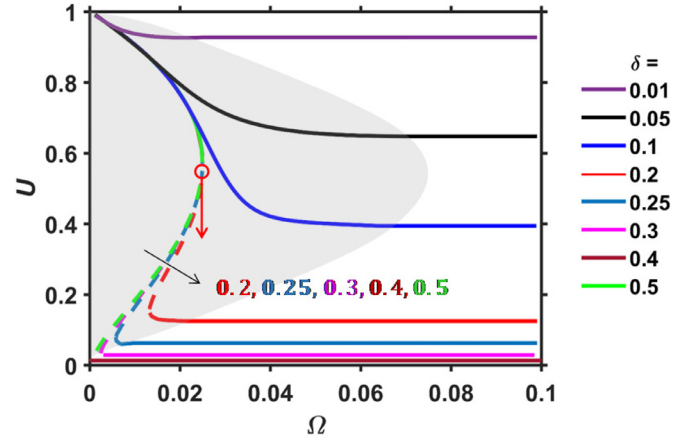
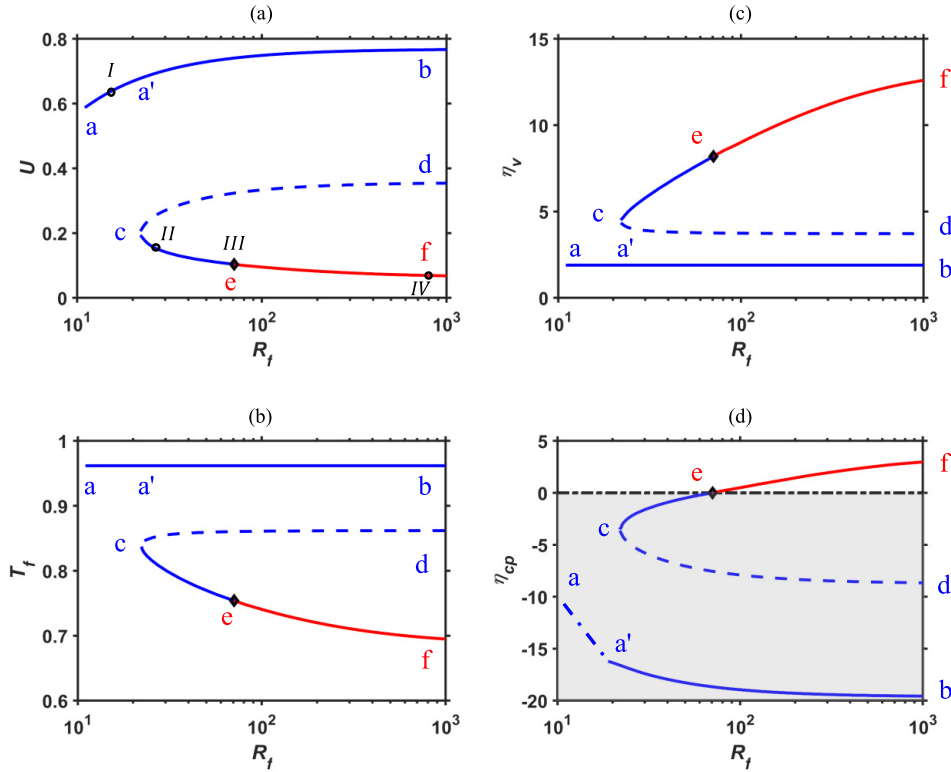


Fig. 3. Change of flame propagation speed with the heat transfer coefficient at different initial droplet mass loadings and  $Le = 1.0$  in planar flames. The open circle indicates the turning point. The shaded area corresponds to the solutions of regime 1, whereas the unshaded one regime 2. Solid lines: stable flames; dashed lines: unstable flames.

For relatively small  $\delta = 0.01$ , with increased  $\Omega$ ,  $U$  first slightly decreases in regime 1 (shaded areas, ECF behind the FF), whilst keeps unchanged in regime 2 (i.e. ECF before the FF). For higher  $\delta$  (e.g. 0.05 or 0.1 in Fig. 3), this decrease is more pronounced in regime 1, but in regime 2  $U$  is still almost constant with lower  $U$ . When  $\delta$  is 0.2–0.3, planar flame speed bifurcates and Z-shaped solutions are observable. There exist three branches, i.e. upper stable (normal) flame with high speed, middle unstable flame and lower stable (weak) flame with low speed. The first two always lie in regime 1, while the last one may in regime 1 or 2. The jump from upper stable flame to lower stable one occurs (denoted by the arrow in Fig. 3), which is also observed from the experimental, numerical and theoretical work in two-phase systems (Ju and Law, 2000; Li et al., 2019; Mitani, 1982b; Modak et al., 2006; Blouquin and Joulin, 1998). The turning points of the reversed C-shaped curves are always located in regime 1 and approximately corresponds to the burning velocity between 0.5 and 0.6, close to the values corresponding to flammability limits predicted by the theoretical analysis (Blouquin and Joulin, 1998) and numerical simulation of two-phase flames (Modak et al., 2006; Yang and Kee, 2002), and also gaseous non-adiabatic flames (Ju et al., 2001).

For even higher  $\delta$  (e.g. 0.4 or 0.5), the reversed C-shaped branches are gradually clustered in regime 1, while the lower weak flame branch tends asymptotically to zero (that for  $\delta = 0.5$  is not shown in Fig. 3). The low-speed weak flame is also observed from the theoretical analysis on planar flames with dispersed water mists (Belyakov et al., 2018) and solid particles (Ju and Law, 2000), thereby confirming the correctness of our model. As shown in Fig. 3, the weak flame is mainly in regime 2, in which it is caused by the evaporative heat loss effects in unburned zones, which is quantified by the pronounced temperature gradients near the FF. With larger  $\delta$  and/or  $\Omega$ , the lower flame branches become weaker, and the gas temperature distributions in the fresh mixtures are more distributed. Accordingly, the temperature gradients near the FF are smaller in the unburned zone (Belyakov et al., 2018), which leads to slower thermal runaway from the chemical reactions and hence a new balance can be established between relatively weak heat release and slow thermal diffusive transport. In the current non-radiative configuration, the planar flame does not show a flammability limit, which is consistent with the findings made by Ju and Law (2000), and Ju et al. (2001). Note that this can be established within the unsteady formulation of the problem. Generally, the droplet properties, i.e.  $\delta$  and  $\Omega$ , have significant



**Fig. 4.** Flame propagation speed (a), temperature (b), evaporation onset front (c) and completion front (d) as functions of flame radius for regime 1 and regime 2 at  $\delta = 0.25$ ,  $\Omega = 0.02$  and  $Le = 1.0$ . Four points in (a), I-IV, are selected for comparisons of their flame structures in Fig. 5. Blue and red lines denote flames in regimes 1 and 2, respectively. The shaded region in (d) corresponds to regime 1 and the remaining region is in regime 2. The continuity of regime 1 and regime 2 is denoted by a black diamond symbol. Solid lines: stable flames; dashed lines: unstable flames. Dashed-dotted line (i.e.  $a-a'$ ): fully dispersed droplet distribution. (For interpretation of the references to color in this figure legend, the reader is referred to the web version of this article.)

influences on planar flame propagation. Since they are the limiting solutions of spherical flames, the results in Fig. 3 would act as the guidance to further explore the bifurcation and multiplicity of two-phase spherical flames based on the model derived in Section 3.

#### 4.2. General bifurcation behavior and structure of droplet-laden spherical flames

Fig. 4a–d show typical results of droplet-laden spherical flames, about  $U$ ,  $T_f$ ,  $\eta_v$  and  $\eta_{cp}$  as functions of  $R_f$  with  $\delta = 0.25$ ,  $\Omega = 0.02$  and  $Le = 1.0$ . In Fig. 4a, an upper normal flame branch and a lower C-shaped branch exist. The former is also observed in the previous theoretical analysis of gaseous-droplet flame in Refs. Han and Chen (2015), Blouquin and Joulin (1998) and Zhuang and Zhang (2019), whilst the latter is new. Based on the fold bifurcation theory (Ju et al., 1997; Thompson and Stewart, 2002), lines  $a-b$  and  $c-e-f$  are stable, while line  $c-d$  unstable. Meanwhile, the blue curves (i.e.  $a-b$ ,  $c-d$ ,  $c-e$ ) correspond to regime 1, while the red ( $e-f$ ) regime 2. We first look at regime 1. Along line  $a-b$ ,  $U$  monotonically increases with  $R_f$  and finally tends to be approximately 0.766 at large  $R_f$  ( $U \approx 0.767$  close to that of planar flame with  $\delta = 0.25$  and  $\Omega = 0.02$  in Fig. 3). The upper flame branch corresponds to the upper branch of flame temperature  $T_f$  and lower branches of EOF and ECF (i.e.  $\eta_v$  and  $\eta_{cp}$ ), see lines  $a-b$  respectively in Fig. 4b–d. The evaporation front evolutions with respect to the FF are the new results from our model and have not been included in the previous theoretical analysis, e.g. (Belyakov et al., 2018; Han and Chen, 2015; Blouquin and Joulin, 1998; Zhuang and Zhang, 2019). It can be seen that the higher  $T_f$ , the smaller  $\eta_v$ , indicating that the droplets start to evaporate closer to the FF, consistent with the findings from Refs. Belyakov et al. (2018) and Zhuang and Zhang (2019). It is no-

ticeable that along the dash-dotted line  $a-a'$  in Fig. 4d,  $\eta_{cp}$  is always equal to  $-R_f$ , indicating that the evaporating droplets fully distributed in the domain when the flame radius is still small ( $< 20$ ). In this case, zone 4 shown in Fig. 2a does not exist. Gradually, ECF arises at the spherical centre in the burned zone, moves outwardly and concentrically with the FF and finally  $\eta_{cp}$  tends to be  $-20$ . This implies that the residual droplets only exist behind the FF with a finite distance for stably propagating spherical flames. For brevity, the upper stable flame branch will be termed as “normal flame” hereafter.

Along line  $c-e$ ,  $U$  and  $T_f$  gradually decrease with  $R_f$ , whereas  $\eta_v$  and  $\eta_{cp}$  have the opposite tendency. The lower the flame temperature  $T_f$ , the farther the EOF in the unburned zone, with respect to the FF. In the meantime, the ECF in the burned zone becomes close to the FF. At  $R_f \approx 70$  (i.e. the critical point “e” shown in Fig. 4), the local droplets critically complete the evaporation at the FF. In the present model, the critical point “e” can be determined with Eqs. (37)–(39). Further outward expansion of the flames leads to the transition from regime 1 to regime 2, and in the latter case the droplets have finished evaporation before they directly interact with the FF. The flame can still propagate to larger radius, with monotonically decreased  $U$  and  $T_f$ , as well as increased  $\eta_v$  and  $\eta_{cp}$  (see lines  $e-f$  shown in Fig. 4a–d). For this branch in regime 2,  $U$  finally tends to 0.067 at  $R_f = 10^3$ , which equals to the value for planar flame when  $\delta = 0.25$  and  $\Omega = 0.02$  as predicted in Fig. 3. We will term the solutions of both lines  $c-e$  and  $e-f$  as “weak flames” in the following analysis, although they may respectively belong to regime 1 and 2 demarcated with the diamond symbol in Fig. 4. Note that here we term them as “weak flames” because they have lower flame propagation speed  $U$  and temperature  $T_f$ , compared to the branch  $a-b$ .

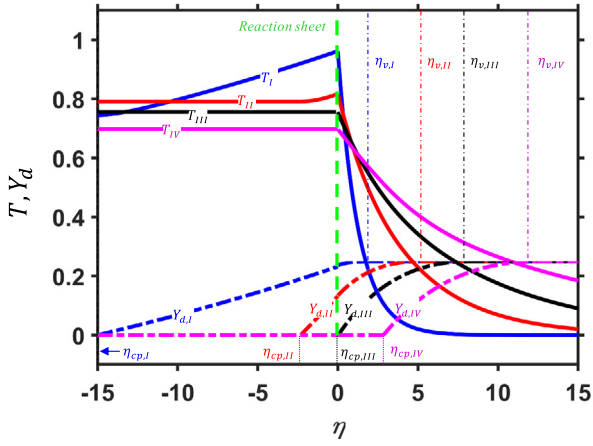


**Fig. 5.** Distributions of temperature and droplet mass loading for points I-IV shown in Fig. 4a. Bold dashed lines: flame fronts ( $\eta = 0$ ); Dashed lines: evaporation fronts ( $\eta_v$  and  $\eta_{cp}$ ). (For interpretation of the references to color in this figure legend, the reader is referred to the web version of this article.)

To compare the flame structures in regimes 1 and 2 in Fig. 4, the spatial distributions of gas temperature and droplet mass loading at four selected solutions (I, II, III and IV marked in Fig. 4a) are plotted in Fig. 5. Note that I is normal flame solution, whilst the rest correspond to the weak flame solutions. Also, I and II are in regime 1, IV in regime 2, and III lies at the transition point. For I, the droplet is fully dispersed in both burned and unburned zones, but the loading  $Y_d$  is comparatively high near the FF. As a normal flame, it has high flame temperature (slightly less than unity), but considerable temperature gradients in both zones. Particularly, for flame I, the high temperature in unburned zone is localized, i.e.  $\eta < 5$  in Fig. 5. For the shown weak flames, the droplets are partially distributed close to the FF in the unburned zone (e.g. II) or only in unburned zone (e.g. IV). Furthermore, the flame temperature is reduced gradually from II to IV, all of which are lower than that of the normal flame I. This is consistent with the tendency revealed from Fig. 4b. The temperature gradients in the burned zone of the weak flames are small or even zero, which implies that the thermal diffusivities towards there would be much smaller than the normal flame. For the unburned zone, temperature gradients also decrease but are still finite. The temperature far from the FF in the unburned zone ( $\eta > 1$ ) increases from I to IV. Accordingly, the EOFs  $\eta_v$  in flames I-IV gradually become far from the FF, as marked in Fig. 5. The similar observations are also made by Belyakov et al. (2018) based on droplet-laden planar flames. Therefore, different regimes are responsible for different heat transport characteristics caused by the distributions of the water droplets. This leads to new features of the droplet-laden spherical flames, particularly weak flames, which will be further discussed in the following. It can also be found from our results (not presented here) that from regime 1 to regime 2 around III, the flame structures smoothly, not abruptly, evolve. Generally, the results in Figs. 4 and 5 confirm the ability of our model to predict the general characteristics of consistently propagating FF and evaporation fronts, as well as the transition between different regimes and droplet distributions.

### 4.3. Spherical flame propagation

#### 4.3.1. Effects of initial droplet mass loading and evaporative heat loss

Fig. 6a–c show the dependencies of flame propagation speed  $U$ , EOF  $\eta_v$  and ECF  $\eta_{cp}$  on flame radius  $R_f$  for  $\Omega = 0.02$  and  $Le = 1.0$ . The effects of various initial droplet mass loadings  $\delta$  are discussed, and the results of  $\delta = 0.25$  from Fig. 4 are also added for comparisons. The upper (lower) normal flame branch in Fig. 6a

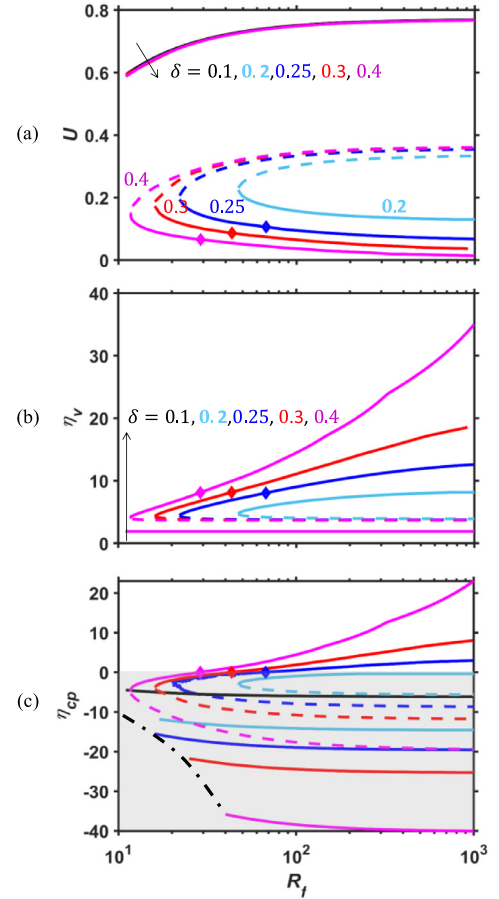


**Fig. 6.** (a) Flame propagation speed, (b) evaporation onset front and (c) completion front as functions of flame radius for different  $\delta$  at  $\Omega = 0.02$  and  $Le = 1.0$ . Legend same as those in Fig. 4. (For interpretation of the references to color in this figure legend, the reader is referred to the web version of this article.)

responds to the lower (upper) branches for  $\eta_v$  and  $\eta_{cp}$  in Fig. 6b and c, respectively. When  $\delta$  is relatively small (e.g. 0.1), only normal flame solutions can be observed. With  $\delta \geq 0.2$ , besides that, a C-shaped curve arises, with intermediate unstable solutions and lower stable weak flame solutions. The turning points of these C-shaped curves are their critical flame radii, at which the outwardly propagating spherical flames can be initiated. The critical flame radii decrease with increased initial droplet loading. This is probably because the larger loading can result in stronger temperature gradient around the FF, and therefore the new balance around the FF between the heat release and the heat diffusive transport can be established in a smaller radius (i.e. with lower volumetric heat loss). For the C-shaped branch, when  $\delta \geq 0.25$ , regime transition occurs at the critical locus (denoted with symbols in Fig. 6), and regime 2 can exist at smaller radius due to increased  $\delta$ . Also, along the weak flame branch,  $U$  is smaller and decreases more quickly with  $R_f$  at larger  $\delta$ . This is justifiable since the stronger cooling effect from larger droplet mass loading would reduce the flame propagation speed.

The EOFs  $\eta_v$  of the normal flames are almost unchanged with  $\delta$  (see Fig. 6b), while their ECFs  $\eta_{cp}$  are closer to the FF with smaller  $\delta$  (see Fig. 6c). This can be explained by the fact that when the initial mass loading is smaller, droplets in a larger domain around the spherical centre can finish the evaporation for the same flame radius. Similar to line  $a-a'$  in Fig. 4, the dash-dotted line in Fig. 6c indicates that at the early phase of spherical flame propagation, droplets can survive in the entire domain at larger flame radius

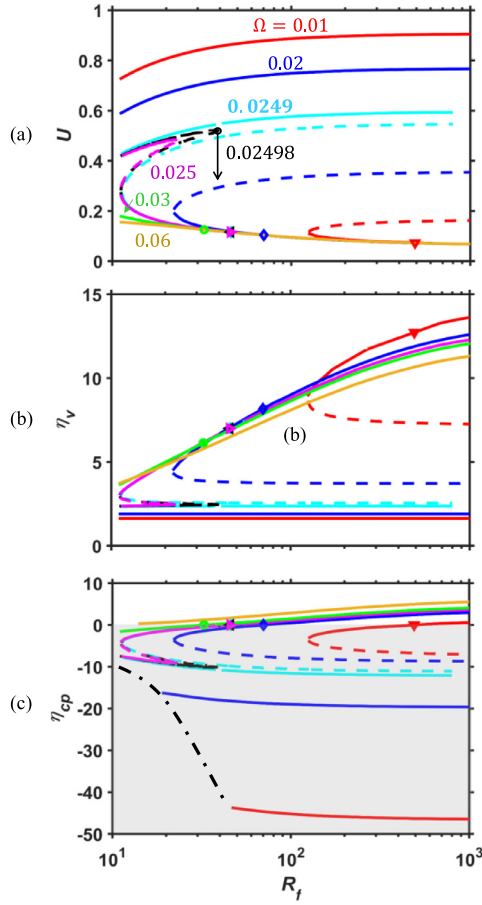


**Fig. 7.** (a) Flame propagation speed, (b) evaporation onset front and (c) completion front as functions of flame radius for different  $\Omega$  at  $\delta = 0.25$  and  $Le = 1.0$ . The arrow in (a) indicates the flame jump transition. Legend same as those in Fig. 4. (For interpretation of the references to color in this figure legend, the reader is referred to the web version of this article.)

with higher  $\delta$ , say about  $\eta_{cp} = -40$  when  $\delta$  is 0.4. However, for the weak flames,  $\eta_v$  increases with  $\delta$ , due to the decreased flame temperature and increased fresh gas temperature (see Fig. 5). For their ECFs  $\eta_{cp}$ , the magnitudes (i.e. the distance off the FF) first decrease (in regime 1) and then increase (in regime 2) when the initial loading is increased. This is because the higher  $\delta$  leads to weaker flames (parameterized by lower  $U$  and  $T_f$ ) due to evaporative heat loss, which correspond to more distributed gas temperatures than those of normal flames, as demonstrated in Fig. 5. This would directly result in longer evaporation time for the droplets subject to their temperature above boiling point, and therefore larger ECFs  $\eta_{cp}$ . Therefore, the initial droplet mass loading considerably influences the flame multiplicity, regime variation as well as the weak flames.

Likewise, Fig. 7a–c show the dependencies of flame propagation speed  $U$ , EOF  $\eta_v$  and ECF  $\eta_{cp}$  on flame radius  $R_f$  for a fixed value of  $\delta = 0.25$  at  $Le = 1.0$ . Here the effects of heat exchange coefficients  $\Omega$  are discussed. In contrast to the  $\delta$  effects on  $U$ - $R_f$  solutions,  $\Omega$  influences both the upper and lower C-shaped branches, i.e. normal and weak flames. Regimes 1 and 2 co-exist in the weak flames in all the shown cases except  $\Omega = 0.06$ , which is entirely in regime 2. As shown in Fig. 7a, with increased  $\Omega$  from 0.01 to 0.0249, the normal flame and the C-shaped branch become close to each other. When  $\Omega = 0.02498$ , they merge into a new  $\tau$ -shaped curve, leading to flame bifurcation (indicated by the arrow in Fig. 7a). Specifically, at the turning point,  $U$  experiences a jump from the nor-

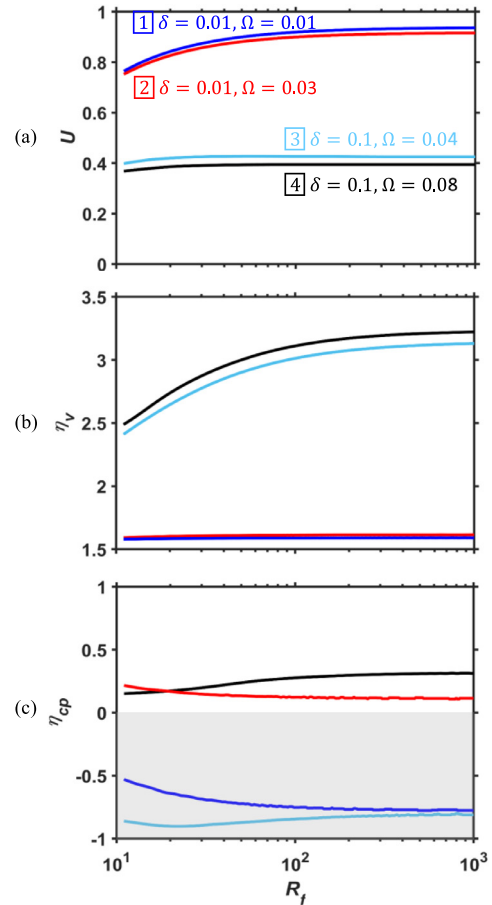


**Fig. 8.** (a) Flame propagation speed, (b) evaporation onset front and (c) completion front as functions of flame radius for different heat exchange coefficients  $\Omega$  at small  $\delta$ . Legend same as those in Fig. 4. (For interpretation of the references to color in this figure legend, the reader is referred to the web version of this article.)

mal flame to the weak flame. Note that this bifurcation occurs in regime 1. This process acts as the re-establishment of the energy balancing between thermal runaway and diffusive transport in regime 1 (heat loss in both burned and unburned zones) and regime 2 (only in unburned zone). This new  $U - R_f$  pattern for flame propagation has not been observed from the previous theoretical analysis in Refs. Han and Chen (2015) and Zhuang and Zhang (2019) for gas-droplet spherical flames. Moreover, the  $\tau$ -shaped curve also exists with  $\Omega = 0.025$ , beyond which ( $\Omega = 0.03$  and 0.06 in Fig. 7) it degrades into a single weak flame branch. These weak flames can propagate at very small radii (e.g.  $\eta = 10$ ) and therefore sustain high stretch. However, whether they evolve from a flame ball, an igniting kernel, or a self-sustaining spherical flame close to flammability limit, as indicated in Refs. Chen and Ju (2007), He (2000), Zhang and Chen (2011), Zhang et al. (2013a) and Zhuang and Zhang (2019), cannot be predicted based on the current model.

The upper (lower) stable flame branch in Fig. 7a corresponds to the lower (upper) branches for  $\eta_v$  and  $\eta_{cp}$  in Fig. 7b and c, respectively. The EOFs of the normal flames are negligibly affected by variable  $\Omega$ . However, their corresponding ECFs in Fig. 7c decrease with  $\Omega$ , since the droplets can be depleted more quickly with stronger evaporation rates. The dash-dotted line in Fig. 7c indicates that full droplet distributions in the burned and unburned zones can persist at larger flame radius when evaporative heat loss is smaller. For the weak flames, both EOFs and ECFs are marginally

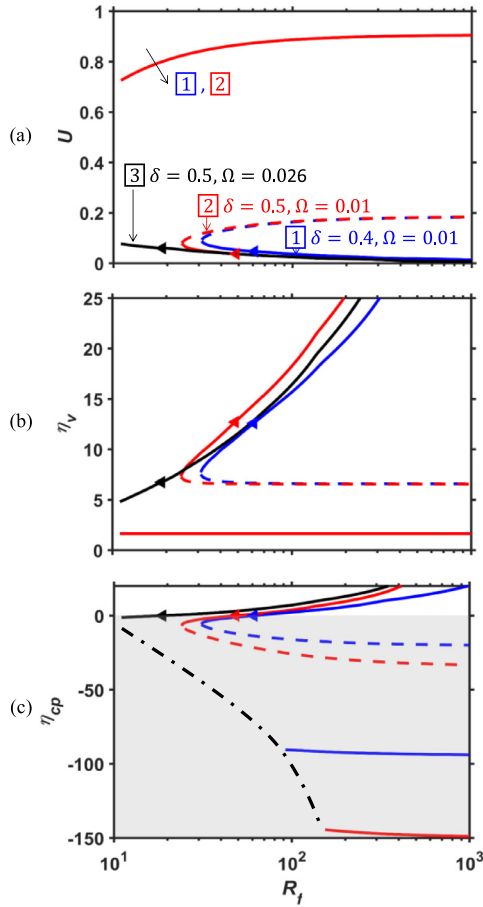


**Fig. 9.** (a) Flame propagation speed, (b) evaporation onset front and (c) completion front as functions of flame radius for different evaporation heat exchange coefficients  $\Omega$  at large  $\delta$ . Legend same as those in Fig. 4. (For interpretation of the references to color in this figure legend, the reader is referred to the web version of this article.)

influenced by  $\Omega$ , compared to the results in Fig. 6 caused by different  $\delta$ .

To further elucidate the combined effects of various droplet properties, i.e.  $\Omega$  and  $\delta$ , on spherical flame propagation, Figs. 8 and 9 demonstrate the  $U - R_f$ ,  $\eta_v - R_f$  and  $\eta_{cp} - R_f$  relations for various  $\Omega$  at very small or very large  $\delta$ . These parameter ranges loosely correspond to the upper and lower parts of the  $U - \Omega$  plane indicated in Fig. 3. As shown in Fig. 8a, at  $\delta = 0.01$ , lines #1 and #2 have the similar  $U - R_f$  curves, in the form of normal flames. Their EOFs  $\eta_v$  are close to each other and almost constant with respect to  $R_f$  (see Fig. 8b). This means that the effects of  $\Omega$  on EOFs are small, consistent with the findings from Fig. 7b. However, it is interesting to find from Fig. 8c that the line #1 is in regime 1, while line #2 is in regime 2, although their  $U - R_f$  and  $\eta_v - R_f$  patterns are similar, and both are normal flames. Note that in Figs. 4, 6 and 7, all the flames in regime 2 are weak, different from the current line #2 in Fig. 8. For lines #3 and #4 with larger  $\delta$  and  $\Omega$ , their propagation speeds are lower, i.e. about 0.4, and they also correspond to regime 1 and regime 2, respectively. In all the cases in Fig. 8, the droplets are partially distributed with finite  $\eta_{cp}$  (no dashed-dotted lines as in Figs. 6 and 7) due to the small initial droplet mass loading considered here.

Fig. 9 shows the counterpart results for relatively large  $\delta$  (0.4 and 0.5), which shows the qualitatively similar behaviours of  $U - R_f$ ,  $\eta_v - R_f$  and  $\eta_{cp} - R_f$  relations as those in Figs. 6 and 7. However, Fig. 9a shows that the weak flames can propagate toward large  $R_f$  at an extremely low speed. Also, different from the results

in Fig. 8a, at the early stage of the spherical flame propagation, full distributions of the water droplets in burned and unburned zones are observed, as denoted with the dash-dotted line in Fig. 9c.

#### 4.3.2. Effects of Lewis number

For the results discussed above, the Lewis number  $Le$  is fixed to be unity. The effects of Lewis number on propagation of gaseous spherical flames are important (Chen and Ju, 2007; Han and Chen, 2015; He, 2000; Zhang et al., 2013a; Zhuang and Zhang, 2019) and therefore will be investigated in the context of two-phase flames in Figs. 10 and 11. Fig. 10 shows the relations of  $U - R_f$ ,  $\eta_v - R_f$  and  $\eta_{cp} - R_f$  with  $Le = 0.8$  and  $1.2$ , and  $\delta = 0.1 - 0.3$ . The results from  $Le = 0.8$  are qualitatively similar to those presented in Fig. 6. However, different from Fig. 6a, in Fig. 10a, along the normal flame branch, the flame propagation speed  $U$  decreases, and tends to 0.766 when  $R_f$  is sufficiently large. This decrease is due to the preferential effects of flame stretch (i.e.  $K \equiv 2U/R_f$  for spherical flames) and small Lewis number ( $< 1$ ) (Law, 2006; Chen and Ju, 2007; Zhang and Chen, 2011; Zhang et al., 2013b). Meanwhile, also because of the foregoing flame enhancement effects, compared to those with same  $\delta$  (say 0.2 or 0.3) in Fig. 6 ( $Le = 1.0$ ), the weak flames can be initiated at larger critical radii in regime 1 (larger volumetric heat loss) with  $Le = 0.8$ . Moreover, its propagating speed monotonically decreases with radius, due to the gradually decreasing flame stretch. Meanwhile, the higher loading  $\delta$  leads to lower propagation speed  $U$  of the weak flames, whilst those of the normal flames are almost not affected by variable  $\delta$ . The relations between  $\eta_v$ ,  $\eta_{cp}$  and  $R_f$  with respect to  $\delta$  in Fig. 10b and c are qualitatively similar to those in Fig. 6.

At  $Le = 1.2$ , considerable differences can be found, compared to  $Le = 1.0$  in Fig. 6. Note that only single regime, regime 1, exists for  $\delta = 0.1$  and  $0.2$ . For  $\delta = 0.3$ , the normal flame is in regime 1, whilst the weak one is in regime 2, as indicated in Fig. 10c. Specifically, only one normal flame branch is observed for  $\delta = 0.1$ , along which  $U$  monotonically increases with  $R_f$ . With larger  $\delta$ , e.g. 0.2 and 0.3,  $U - R_f$  curves have two separate branches: upper C-shaped one and a lower stable weak flame branch. For the normal flames, they can only propagate beyond a critical flame radius, since the Lewis number effects become comparatively small. For the weak flames discussed here, they are in ( $\delta = 0.2$ ) or close to ( $\delta = 0.3$ ) regime 2. Both can exist from small to large radii. Their speeds  $U$  show monotonic increase ( $\delta = 0.2$ ) or first increase and then decrease towards a constant value ( $\delta = 0.3$ ). These are not observed in the results above, e.g. in Figs. 4, 6 and 7. For their existence at small radii, the flame temperature and its gradient at the fresh gas side are relatively low. This to some degree offsets the stronger thermal conduction caused by the larger Lewis number (and therefore larger thermal diffusivity). When they further propagate outwardly, the effects of Lewis number and temperature gradient compete: if the former dominates, then the propagation speed of weak flame can monotonically increase, e.g.  $\delta = 0.2$ ; if the later, it demonstrates slightly non-monotonic behaviours as seen from the results of  $\delta = 0.3$ .

Fig. 11 shows the results with  $Le = 0.8$  and  $1.2$ , but with variable evaporation heat loss coefficients  $\Omega$ , i.e. 0.01–0.03. Compared to Fig. 7, the effects of increased  $\Omega$  on the curves of  $U - R_f$ ,  $\eta_v - R_f$  and  $\eta_{cp} - R_f$  are similar, including the flame bifurcation and different regimes. Nevertheless, in Fig. 11a, the normal flame propagation speed decreases with the flame radius due to the decreasing enhancement from the combined effects of Lewis number and positive stretch rate. Therefore, for large  $\Omega$  (say 0.03), Z-shaped curve can be seen, instead of the  $\tau$ -shaped one in Fig. 7. At the upper turning point of this curve, the flame jumps suddenly from normal flame to weak one in the same regime, i.e. regime 1, and finally transits to regime 2 at a larger radius (denoted by the symbols). In fact, this kind of Z-shaped curve can also be observed for

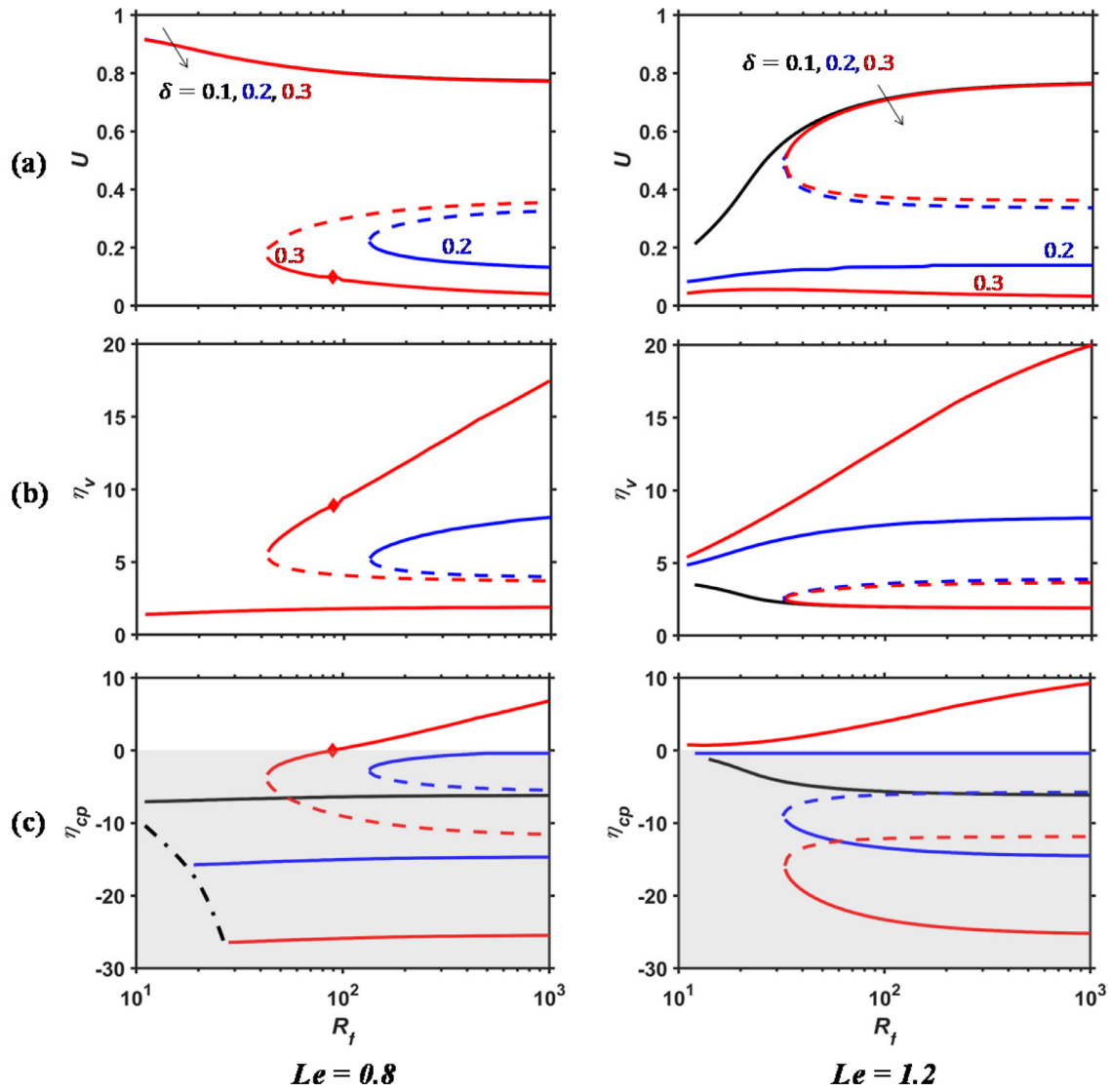


**Fig. 10.** (a) Flame propagation speed, (b) evaporation onset front and (c) completion front as functions of flame radius for different  $\delta$  at  $\Omega = 0.02$  with  $Le = 0.8$  (left) and 1.2 (right). Legend same as those in Fig. 4. (For interpretation of the references to color in this figure legend, the reader is referred to the web version of this article.)

$\Omega = 0.025$  in Fig. 11 (the turning point is beyond  $R_f = 10^3$ , hence not shown here). Interestingly, different from that of  $\Omega = 0.03$ , in this scenario, the flame directly jumps from normal flame in regime 1 into weak flame in regime 2, because the radius at the turning point (beyond  $R_f = 10^3$ ) is larger than that at the critical transition point ( $R_f \approx 10^2$ ). It can be observed from the results of  $Le = 1.2$  that the  $U - R_f$  solutions of  $\Omega = 0.01$  are characterized by a (unclosed) C-shaped branch and a lower weak flame branch. However, there is only one weak flame branch for larger  $\Omega$ , i.e. 0.025 and 0.03. The evolutions of EOFs and ECFs with respect to FFs in Fig. 11b and c for  $Le = 0.8$  and 1.2 are generally similar to those in Fig. 7 with unity Lewis number.

#### 4.4. Stretch rate and Markstein length

Due to the multiple regimes seen from the above analysis, how they respond to the stretch rate merits further discussion. Therefore, the Markstein length ( $L$ ) will be discussed in the following, to quantitatively assess the influence of stretching on the normal and weak droplet-laden spherical flames (Law, 2006). For spherical flames with low stretch ( $R_f \gg 1$  or  $K \ll 1$ ), the following relation holds between flame propagation speed  $U$  and flame stretch  $K$

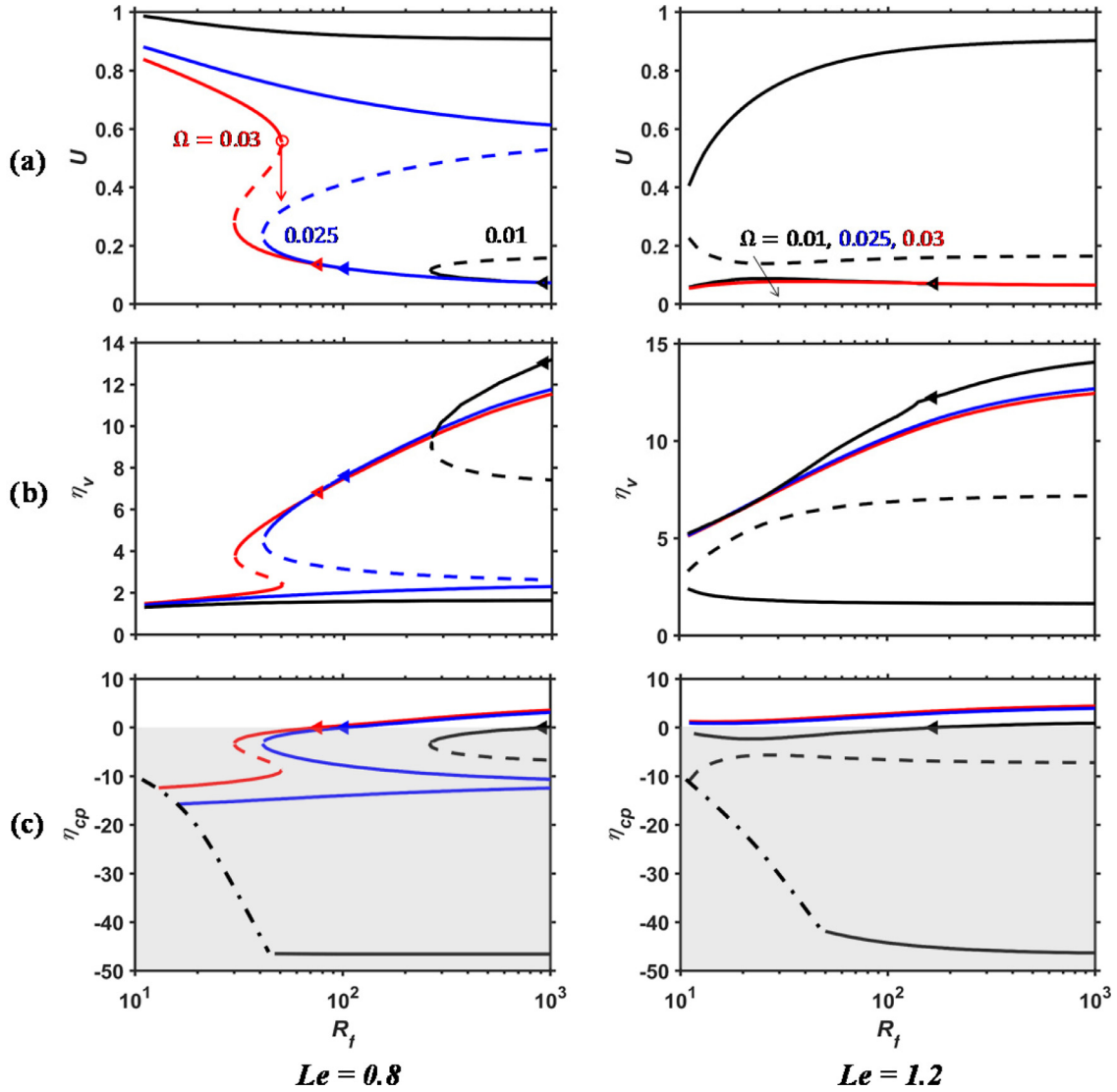
(Law, 2006; Clavin, 1985)

$$U = U^0 - L \cdot K, \quad (40)$$

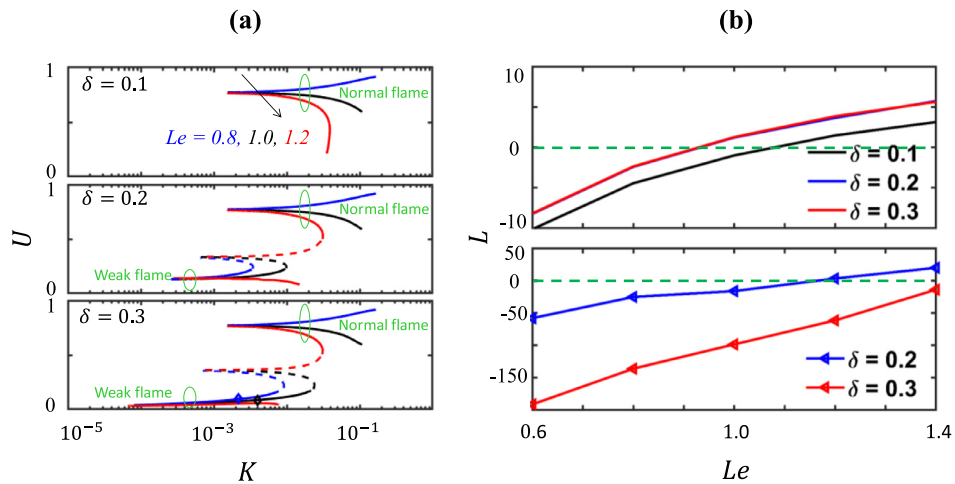
where  $U^0$  is the flame speed at zero stretch rate (i.e. for planar flame at  $R_f \rightarrow \infty$ ). For spherical flames,  $K$  can be derived from  $K \equiv 2U/R_f$ . The Markstein length  $L$  essentially is the slope of the  $U-K$  curve when  $K$  tends to be zero.

Fig. 12a shows the  $U - K$  curves for different droplet mass loadings  $\delta$  at  $\Omega = 0.02$ . The corresponding  $U - R_f$  solutions have been discussed in Figs. 6 and 10. For outwardly spherical flames, the larger the flame radius, the lower the stretch rate. When  $\delta = 0.1$ ,  $U$  of the normal flames is shown to increase (decrease) with the stretch rate for  $Le = 0.8$  ( $Le = 1.0$  and 1.2), which explains the difference of  $U - R_f$  solutions for  $Le = 0.8$  (see Fig. 10), 1.0 (Fig. 6) and 1.2 (Fig. 10) for  $10^1 < R_f < 10^2$ . When  $\delta$  increases to 0.2, the  $U - K$  curves of the normal flames have the similar variations to those with  $\delta = 0.1$ . However, in those of weak flames with  $Le = 0.8$  and 1.0, there exists a maximum  $K$ , beyond which no propagating spherical flames are observable. For larger  $\delta$ , e.g. 0.3, the  $U - K$  curves are similar to those of  $\delta = 0.2$ .

Fig. 12b shows the dependence of the Markstein length,  $L$ , on the Lewis number,  $Le$ , for different initial loadings  $\delta$  at  $\Omega = 0.02$ .



**Fig. 11.** (a) Flame propagation speed, (b) evaporation onset front and (c) completion front as functions of flame radius for different heat exchange coefficients  $\Omega$  at  $\delta = 0.25$  with  $Le = 0.8$  (left) and 1.2 (right). The arrow in (a) indicates the flame jump transition. Legend same as those in Fig. 4. (For interpretation of the references to color in this figure legend, the reader is referred to the web version of this article.)



**Fig. 12.** (a) Flame propagating speed  $U$  as a function of stretch rate  $K$  for different droplet mass loadings  $\delta$  at  $\Omega = 0.02$ ; (b) Markstein length  $L$  as a function of Lewis number  $Le$  for normal flame (upper) and weak flame (lower) with different droplet mass loadings  $\delta$  at  $\Omega = 0.02$ .

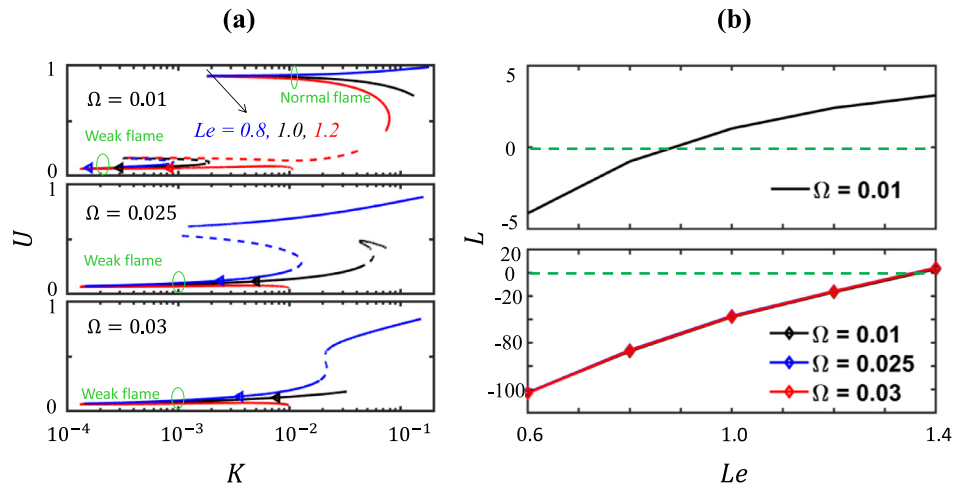


**Fig. 13.** (a) Flame propagating speed  $U$  as a function of stretch rate  $K$  for different heat exchange coefficients  $\Omega$  at  $\delta = 0.25$ ; (b) Markstein length  $L$  as a function of Lewis number  $Le$  for normal flame (upper) and weak flame (lower) with for different heat exchange coefficients  $\Omega$  at  $\delta = 0.25$ .

The upper sub-figure in Fig. 12b corresponds to the normal flame in Fig. 12a, and the lower one corresponds to the weak flame. For the normal flames with different  $\delta$ ,  $L$  is negative at small  $Le$ , whereas is positive for large  $Le$ . This indicates that under small (large)  $Le$  conditions, the flame propagation speed would be enhanced (reduced) compared to the unstretched flame speed  $U^0$ . This observation is consistent with that from the previous work for gaseous and two-phase spherical flames (Han and Chen, 2015; Zhang et al., 2013b). Meanwhile, the magnitudes of  $L$  become smaller when  $Le$  is close to unity, indicating that the extent of enhancement or reduction tends to be small. Moreover, for small (large)  $Le$ , with increased  $\delta$  from 0.1 to 0.2, the magnitudes of  $L$  decrease (increase). Nevertheless, for the entire range of  $Le$ , when  $\delta$  is beyond 0.2, the variation of the Markstein length is negligibly small.

For the weak flames, Markstein length  $L$  is mainly negative for the considered droplet mass loading, except for  $Le > 1.2$  when  $\delta = 0.2$ . This physically means that the propagation speed  $U$  of the weak flame would mainly be enhanced for most of the shown Lewis numbers. When  $Le$  increases, the magnitudes of  $L$  decrease, and therefore the enhancement is gradually minimized. Since most of the weak flames fall category into as regime 2, the variations of single-sided temperature gradients near the FF at the fresh mixture zone considerably affect the thermal diffusive transport. Meanwhile, the magnitudes of  $L$  for the weak flames are generally larger than those for the normal flames. When it comes to the effects of initial droplet mass loading, generally, larger  $\delta$  leads to larger magnitudes of the Markstein length  $L$ , which means the stronger stretch effects on spherical flames.

Similarly, Fig. 13 shows the results for different heat exchange coefficients  $\Omega$  at  $\delta = 0.25$ . The corresponding  $U$ - $R_f$  solutions have already been shown in Figs. 7 and 11. In Fig. 13a, the  $U$ - $K$  curves with  $\Omega = 0.01$  are similar to those in Fig. 12a. For  $\Omega = 0.025$  and  $0.03$ , the normal flame disappears or jump to the weak flame; instead, only one weak flame branch is present, as shown in Fig. 13a. Also, for the upper branch, it can be observed from Fig. 13b that  $L$ - $Le$  relation resembles that in Fig. 12b, although here only under the condition of  $\Omega = 0.01$  have we the normal flame solutions. However, the influence of heat exchange coefficient  $\Omega$  on the  $L$ - $Le$  curves for weak flames is negligible, different from that of droplet mass loadings  $\delta$  indicated in Fig. 12b.

#### 4.5. Typical flame bifurcation and multiplicity

Flame bifurcations and multiplicity have been shown in the previous sections. The typical kinds of flame bifurcation exist in the two-phase propagating spherical flame are summarized here. Twelve patterns are identified in terms of the droplet spatial distributions (i.e. "regime") and gases flame (i.e. "stable/unstable" as well as "normal/weak") characteristics, and listed individually in Fig. 14, which will be further interpreted below.

Pattern (1) is normal flame in regime 1. This pattern only has one stable branch and it can be observed at low droplet mass loading ( $\delta$ ) with small heat transfer coefficient ( $\Omega$ ). In this pattern, the EOF is close to the FF in unburned zone, but the ECF is in burned zone (partially dispersed droplets) or no ECFs (fully dispersed droplets).

Pattern (2) is in regime 1 with intermediate propagation speed. Compared to pattern (1), this pattern occurs for higher  $\delta$  and  $\Omega$ . Although the EOF is relatively far from the FF, nevertheless, droplets are still fully or partially distributed in the burned zone, due to larger  $\delta$ .

Pattern (3) is in regime 1, and consists of two stable flame branches, i.e. the upper normal and the lower weak flame (within a C-shaped curve). Compared to pattern (2), this bifurcation occurs for higher  $\delta$  and lower  $\Omega$ .

Pattern (4) is in regime 1 or regime 2 with a transition point. This pattern is a successor to pattern (3) as  $\delta$  increases. Along the lower weak branch, the flame undergoes the smooth change from regimes 1 to 2, depending on the movement of the ECF relative to the FF.

Pattern (5) is in regime 1 or regime 2 as  $\tau$ -shaped curve. This pattern is a successor to pattern (4) as  $\Omega$  increases. The normal flame jumps into the weak flame at a critical radius, but both are in regime 1.

Pattern (6) is in regime 1 or regime 2 and has only one lower flame branch. Similarly, this pattern is the successor to pattern (5) as  $\Omega$  increases.

Pattern (7) evolves from pattern (4) with Lewis number above unity, whereas patterns (8) and (9) evolve from pattern (5) with Lewis number below unity (reversed S-shaped curve). In the former, the normal flame jumps into weak flame in regime 1. Conversely, the latter shows the bifurcation from normal flame in regime 1 into weak flame in regime 2. Patterns (10)-(12) are

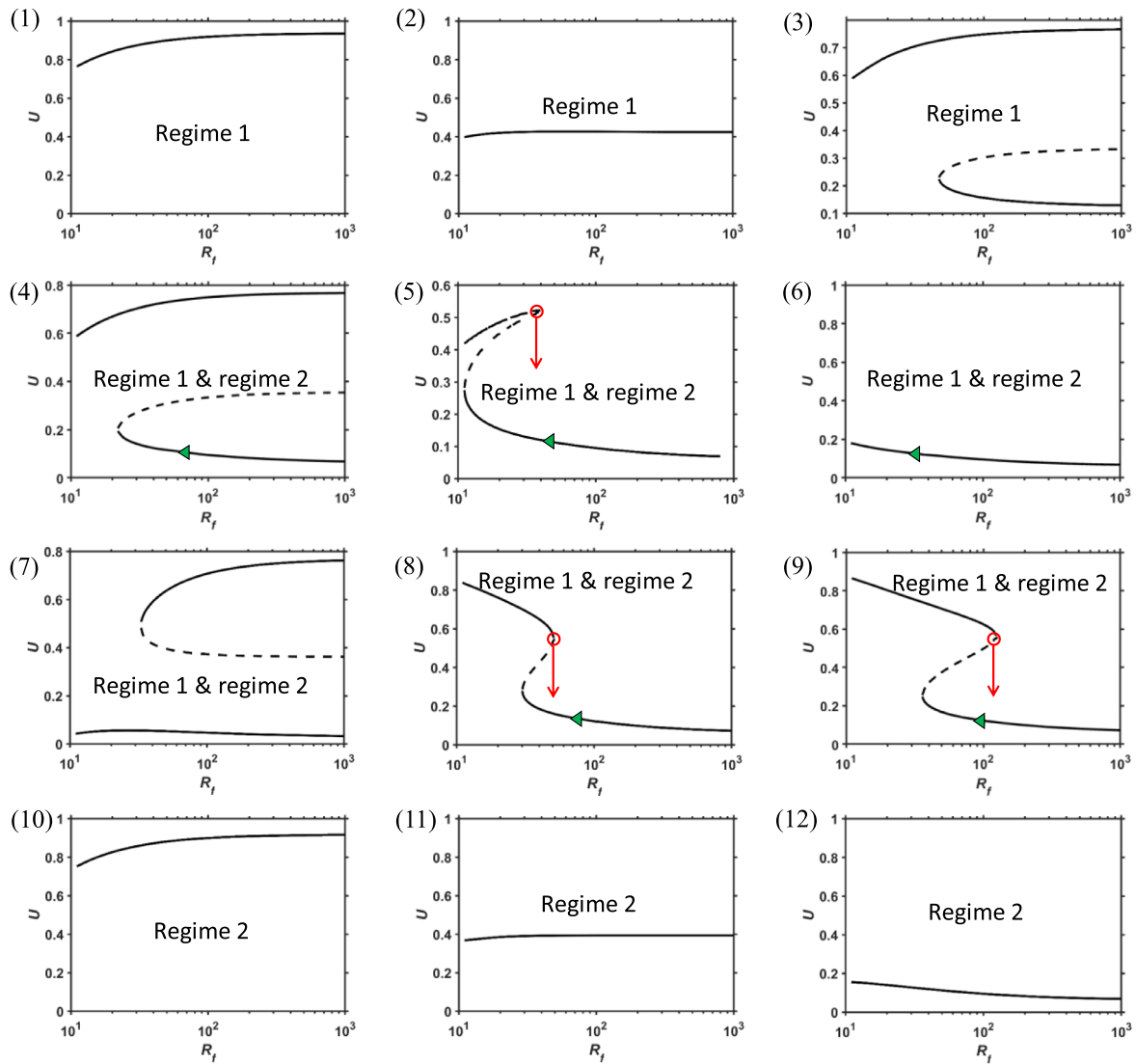


**Fig. 14.** Typical kinds of flame bifurcation and multiplicity of the two-phase premixed spherical flames. The arrows in (5), (8) and (9) indicate the flame jump. Legend same as those in Fig. 4. (For interpretation of the references to color in this figure legend, the reader is referred to the web version of this article.)

normal, intermediate and weak flames, respectively, and are all in regime 2.

## 5. Conclusions

In the present work, we develop a general theoretical model for outwardly propagating spherical flames with water droplets. Correlations describing flame propagation speed, flame temperature, droplet distribution and flame radius are derived, based on the assumptions of constant density, quasi-steadiness, low stretch and large activation energy. With these correlations, the influences of initial droplet mass loading, evaporation heat loss and Lewis number on droplet-laden spherical flames are investigated. Meanwhile, our model can generally predict different flame types (weak or normal flames), flame stability (stable or unstable flames) and droplet distributions (full or partial dispersion), as well as the bifurcations and transitions between the above distinct flame solutions.

The outwardly spherical flame propagation is strongly affected by water droplet properties, i.e. initial droplet mass loadings ( $\delta$ ) and heat exchange coefficients ( $\Omega$ ). When  $\delta$  and  $\Omega$  are relatively small, there is only one normal stable flame. For increased val-

ues of  $\delta$  and  $\Omega$ , two stable flames arise: normal and weak flames, respectively. For a fixed  $\Omega$ , increased  $\delta$  mainly affects the weak flame, leading to decreased flame propagation speed, increased values of evaporation onset and completion fronts. However, for a fixed  $\delta$ , increased  $\Omega$  affects both normal and weak flames and flame bifurcation is observed for large  $\Omega$ . Different droplet properties also greatly influence the weak flame transition between different regimes.

Our results also show that the Lewis number also has significant influence on spherical flame propagation, in terms of flame bifurcation and regime transition. The Lewis number would affect the flame propagation jointly with the positive stretch rate and/or the evolving temperature gradients along the flame front through the interactions with the dispersed evaporating droplets. In addition, the magnitudes of Markstein length of the normal flames are shown to decrease when the Lewis number approaches unity. However, those of weak flames are mostly negative, indicating the enchantment for the shown Lewis number range. The generally larger magnitudes of Markstein length of weak flames indicate stronger sensitivity to stretch compared to those of normal flames.

Despite the above rich findings from our model, it should be acknowledged that assumptions (e.g. constant thermal properties

and quasi-planar flames) are introduced to perform the foregoing theoretical analysis. Naturally, the conclusions drawn are only valid for the problems where these assumptions hold. As our future work, theoretical analysis through relaxing some of the above assumptions and/or detailed numerical simulations will be conducted to investigate propagation of two-phase spherical flames.

### Declarations of Competing Interest

None.

### CRedit authorship contribution statement

**Yijie Zhuang:** Methodology, Formal analysis, Writing - original draft. **Huangwei Zhang:** Writing - original draft, Writing - review & editing, Funding acquisition, Project administration.

### Acknowledgements

YZ is financially supported by the start-up grant (22041375601) from GDUT. HZ is financially supported by the research grant (R-265-000-604-133) from NUS.

### Supplementary materials

Supplementary material associated with this article can be found, in the online version, at doi:10.1016/j.ijmultiphaseflow.2020.103220.

### References

- Babushok, V.I., Linteris, G.T., Baker, P.T., 2015. Influence of water vapor on hydrocarbon combustion in the presence of hydrofluorocarbon agents. *Combust. Flame* 162, 2307–2310.
- Bechtold, J., Cui, C., Matalon, M., 2005. The role of radiative losses in self-extinguishing and self-wrinkling flames. *Proc. Combust. Inst.* 30, 177–184.
- Bechtold, J.K., Matalon, M., 1987. Hydrodynamic and diffusion effects on the stability of spherically expanding flames. *Combust. Flame* 67, 77–90.
- Belyakov, N.S., Babushok, V.I., Minaev, S.S., 2018. Influence of water mist on propagation and suppression of laminar premixed flame. *Combust. Theory Model.* 22, 394–409.
- Blouquin, R., Joulin, G., 1998. On the quenching of premixed flames by water sprays: influences of radiation and polydispersity. *Symp. Combust.* 27, 2829–2837.
- Bradley, D., Lawes, M., Liao, S., Saat, A., 2014. Laminar mass burning and entrainment velocities and flame instabilities of 1-octane, ethanol and hydrous ethanol/air aerosols. *Combust. Flame* 161 (6), 1620–1632.
- Chen, Z., 2010. Effects of radiation and compression on propagating spherical flames of methane/air mixtures near the lean flammability limit. *Combust. Flame* 157, 2267–2276.
- Chen, Z., Burke, M.P., Ju, Y., 2009. Effects of Lewis number and ignition energy on the determination of laminar flame speed using propagating spherical flames. *Proc. Combust. Inst.* 32, 1253–1260.
- Chen, Z., Burke, M.P., Ju, Y., 2011. On the critical flame radius and minimum ignition energy for spherical flame initiation. *Proc. Combust. Inst.* 33, 1219–1226.
- Chen, Z., Ju, Y., 2007. Theoretical analysis of the evolution from ignition kernel to flame ball and planar flame. *Combust. Theory Model.* 11, 427–453.
- Chung, S.H., Law, C.K., 1988. An integral analysis of the structure and propagation of stretched premixed flames. *Combust. Flame* 72, 325–336.
- Clavin, P., 1985. Dynamic behavior of premixed flame fronts in laminar and turbulent flows. *Prog. Energy Combust. Sci.* 11, 1–59.
- Crowe, C.T., Schwarzkopf, J.D., Sommerfeld, M., Tsuji, Y., 2011. *Multiphase Flows with Droplets and Particles*, second ed CRC Press, Boca Raton.
- Dvorjetski, A., Greenberg, J.B., 2002. Analysis of extinction of counterflow polydisperse spray diffusion flames by a polydisperse water spray. *Combust. Inst.* 29, 385–392.
- Dvorjetski, A., Greenberg, J.B., 2004. Theoretical analysis of polydisperse water spray extinction of opposed flow diffusion flames. *Fire Saf. J.* 39, 309–326.
- Frankel, M.L., Sivashinsky, G.I., 1984. On quenching of curved flames. *Combust. Sci. Technol.* 40 (1984), 257–268.
- Grant, G., Brenton, J., Drysdale, D., 2000. Fire suppression by water sprays. *Prog. Energy Combust. Sci.* 26, 79–130.
- Greenberg, J.B., 2007. Finite-rate evaporation and droplet drag effects in spherical flame front propagation through a liquid fuel mist. *Combust. Flame* 148, 187–197.
- Greenberg, J.B., Silverman, I., Tambour, Y., 1996. A new heterogeneous burning velocity formula for the propagation of a laminar flame front through a polydisperse spray of droplets. *Combust. Flame* 104, 358–368.
- Han, W., Chen, Z., 2015. Effects of finite-rate droplet evaporation on the ignition and propagation of premixed spherical spray flame. *Combust. Flame* 162, 2128–2139.
- Han, W., Chen, Z., 2016. Effects of finite-rate droplet evaporation on the extinction of spherical burner-stabilized diffusion flames. *Int. J. Heat Mass Transf.* 99, 691–701.
- Hayashi, S., Kumagai, S., 1975. Flame propagation in fuel droplet-vapor-air mixtures. *Symp. Combust.* 15, 445–452.
- He, L., 2000. Critical conditions for spherical flame initiation in mixtures with high Lewis numbers. *Combust. Theory Model.* 4, 159–172.
- Ingram, J.M., Averill, A.F., Battersby, P., Holborn, P.G., Nolan, P.F., 2013. Suppression of hydrogen / oxygen / nitrogen explosions by fine water mist containing sodium hydroxide additive. *Int. J. Hydrog. Energy* 38 8002–2010.
- Joulin, G., Clavin, P., 1979. In: *Linear Stability Analysis of Nonadiabatic Flames: Diffusional-Thermal Model*, 3, pp. 139–153.
- Ju, Y., Guo, H., Maruta, K., Liu, F., 1997. On the extinction limit and flammability limit of non-adiabatic stretched methane-air premixed flames. *J. Fluid Mech.* 342, 315–334.
- Ju, Y., Law, C.K., 2000. Dynamics and extinction of non-adiabatic particle-laden premixed flames. *Proc. Combust. Inst.* 28, 2913–2920.
- Ju, Y., Maruta, K., Niioka, T., 2001. Combustion limits. *Appl. Mech. Rev.* 53, 257–277.
- Law, C.K., 2006. *Combustion Physics*. Cambridge University Press, New York.
- Lee, S., Ha, H., Dunn-rankin, D., Chae, O., 2017. Effects of pressure on structure and extinction limits of counter flow nonpremixed water-laden methane/air flames. *Energy* 134, 545–553.
- Lentati, A.M., Chelliah, H.K., 1998. Physical, thermal, and chemical effects of fine-water droplets in extinguishing counterflow diffusion flames. *Symp. Combust.* 27, 2839–2846.
- Li, H., Zhang, H., Chen, Z., 2018. Effects of endothermic chain-branching reaction on spherical flame initiation and propagation. *Combust. Theory Model.* 23, 496–514.
- Li, Q., Liu, C., Zhang, H., Wang, M., Chen, Z., 2019. Initiation and propagation of spherical premixed flames with inert solid particles. submitted to. *Combust. Theory Model.* Under review.
- Liu, Z., Kim, A., 2000. A review of water mist fire suppression systems—fundamental studies. *J. Fire Prot. Eng.* 10, 32–50.
- Mitani, T., 1982. Comparison of experiments and theory on heterogeneous flame suppressants. *Proc. Combust. Inst.* 19, 869–875.
- Modak, A.U., Abbud-Madrid, A., Delplanque, J.P., Kee, R.J., 2006. The effect of mono-dispersed water mist on the suppression of laminar premixed hydrogen-, methane-, and propane-air flames. *Combust. Flame* 144, 103–111.
- Naito, H., Uendo, T., Saso, Y., Kotani, Y., Yoshida, A., 2011. Effect of fine water droplets on extinguishment of diffusion flame stabilized in the forward stagnation region of a porous cylinder. *Proc. Combust. Inst.* 33, 2563–2571.
- Padilla, R.E., Escofet-martin, D., Pham, T., Pitz, W.J., Dunn-rankin, D., 2018. Structure and behavior of water-laden CH<sub>4</sub> / air counterflow diffusion flames. *Combust. Flame* 196, 439–451.
- Ranz, W.E., Marshall Jr., W.R., 1952. Vaporation from drops, Part I. *Chem. Eng. Prog.* 48, 141–146.
- Ronney, P., Sivashinsky, G., 1989. A theoretical study of propagation and extinction of nonsteady spherical flame fronts. *SIAM J. Appl. Math.* 49, 1029–1046.
- Sakurai, I., Suzuki, J., Kotani, Y., Naito, H., Yoshida, A., 2013. Extinguishment of propane/air co-flowing diffusion flames by fine water droplets. *Proc. Combust. Inst.* 34, 2727–2734.
- Sarkar, S., Mukhopadhyay, A., Sen, S., 2019. Numerical investigation of the effects of polydisperse water sprays on extinction conditions of counterflow methane non-premixed flames. *Combust. Theory Model.* 1–25.
- Sasongko, M.N., Seo, T., Mikami, M., 2016. Extinction condition of counterflow spray diffusion flame with polydisperse water spray. *Fire Saf. J.* 82, 23–29.
- Sazhin, S.S., 2006. Advanced models of fuel droplet heating and evaporation. *Prog. Energy Combust. Sci.* 32, 162–214.
- Seshadri, K., 1978. Structure and extinction of laminar diffusion flames above condensed fuels with water and nitrogen. *Combust. Flame* 33, 197–215.
- Thimothee, R., Chauveau, C., Halter, F., Gokalp, I., 2017. Experimental investigation of the passage of fuel droplets through a spherical two-phase flame. *Proc. Combust. Inst.* 36 (2), 2549–2557.
- Thompson, J.M.T., Stewart, H.B., 2002. *Nonlinear Dynamics and Chaos*. John Wiley & Sons.
- Vicariotto, M., Dunn, D., 2018. Temperature profiles and extinction limits of a coflow water - vapor laden methane / air diffusion flame. *Exp. Fluids* 59, 1–10.
- Yang, W., Kee, J., 2002. The Effect of monodispersed water mists on the structure, burning velocity, and extinction behavior of freely. *Combust. Flame* 130, 322–335.
- Yang, W., Parker, T., Ladouceur, H.D., Kee, R.J., 2004. The interaction of thermal radiation and water mist in fire suppression. *Fire Saf. J.* 39, 41–66.
- Yoshida, A., Kashiwa, K., Hashizume, S., Naito, H., 2015. Inhibition of counterflow methane/air diffusion flame by water mist with varying mist diameter. *Fire Saf. J.* 71, 217–225.
- Yoshida, A., Takasaki, R., Kashiwa, K., Naito, H., Saso, Y., 2013. Extinguishment of counterflow methane / air diffusion flame by polydisperse fine water droplets. *Combust. Flame* 160, 1357–1363.
- Zhang, H., Chen, Z., 2011. Spherical flame initiation and propagation with thermally sensitive intermediate kinetics. *Combust. Flame* 158, 1520–1531.
- Zhang, H., Guo, P., Chen, Z., 2013. Critical condition for the ignition of reactant mixture by radical deposition. *Proc. Combust. Inst.* 34, 3267–3275.
- Zhang, H., Guo, P., Chen, Z., 2013. Outwardly propagating spherical flames with thermally sensitive intermediate kinetics and radiative loss. *Combust. Sci. Technol.* 185, 226–248.
- Zhuang, Y., Zhang, H., 2019. Effects of water droplet evaporation on initiation, propagation and extinction of premixed spherical flames. *Int. J. Multiph. Flow* 117, 114–129.